NEUROSCIENCE

Intrinsic cellular persistent firing sustains hippocampal spatial representations during working memory

Babak Saber Marouf[1,2,3], Antonio Reboreda[1,2], Frederik Theissen[1,2], Rahul Kaushik[4]†, Magdalena Sauvage[1,5,6], Alexander Dityatev[4,5,6], Motoharu Yoshida[1,2,6]*

Copyright © 2026 The Authors, some rights reserved; exclusive licensee American Association for the Advancement of Science. No claim to original U.S. Government Works. Distributed under a Creative Commons Attribution License 4.0 (CC BY).

Neurons are the fundamental units of cognitive processing. The prevailing view holds that neurons are input-output units that fire action potentials only upon receiving sufficient synaptic input. Here, we demonstrate that this may not be the sole operational mode of neurons in vivo during cognitive tasks, by showing that hippocampal place cells actively maintain firing and preserve spatial information through molecularly defined intrinsic mechanisms. Using in vitro and in vivo recordings coupled with molecular manipulation in mice, we reveal that hippocampal persistent firing during spatial working memory is supported by individual neurons via TRPC4 ion channels. Despite the general belief that persistent activity maintains working memory content, we demonstrate that persistent firing instead maintains immediate spatial representations, potentially supporting the encoding of spatial information to guide behavior. These findings position individual neurons as active contributors to information retention, extending their traditional role as passive input-output units and potentially broadening our understanding of neural computation.

INTRODUCTION

Precise maintenance of internal representations in the brain is critical for executing cognitive tasks (*1*, *2*). A potential cellular correlate for this process is persistent neural firing, in which information is maintained by continuous activation of a specific subset of cells (*3*, *4*). Persistent firing has been observed across multiple brain regions—including the prefrontal cortex, hippocampus, and sensory association areas—and is thought to support a wide range of cognitive functions such as working memory, decision-making, attention, spatial navigation, and goal-directed behavior (*2*, *5*–*10*). In the rodent hippocampus, in addition to "time cells" that activate sequentially during relatively short delay intervals (~10 s) (*11*, *12*), a recent study has identified persistently firing cells that span the entire delay period (~30 s) in the mouse hippocampal CA1, outlasting the time-cell sequence (*13*).

Building on the foundational concepts of Lorente de Nó and Hebb, persistent activity has traditionally been attributed to reverberatory dynamics within recurrent synaptic networks (*14*, *15*). This view aligns with the prevailing model of neurons as passive elements generating action potentials only when synaptic inputs exceed a threshold. However, these pure network models often exhibit instabilities such as noise-induced drift and runaway excitation (*3*), and their performance depends on a degree of synaptic fine-tuning rarely observed in biological systems (*4*, *16*). Consequently, these models often struggle to replicate the robust, long-lasting persistent firing observed in biological systems without incorporating additional stabilizing mechanisms (*17*).

Neuromodulators such as acetylcholine, which is vital for working memory and other cognitive functions, can transform the way neurons respond to input signals (*18*). In vitro studies have indicated that individual neurons can continue firing after a brief trigger under the influence of acetylcholine through an intrinsic cellular mechanism—a phenomenon referred to here as "intrinsic persistent firing" (*19*–*24*). We and others have identified TRPC channels as key mediators of intrinsic persistent firing in CA1 pyramidal cells (*20*, *25*). Theoretical studies have demonstrated potential roles for this cellular property in working memory and spatial coding (*26*, *27*). Indeed, incorporating mechanisms of intrinsic persistent firing endows attractor network models with the high stability and robustness observed in in vivo data (*28*–*30*). However, whether intrinsic persistent firing influences in vivo neural activity, sustains information, and supports cognitive function remains unclear because the effects of disrupting this property have not been examined in living animals (*31*, *32*). As a consequence, current computational models—from classical attractor networks to the artificial neural networks underlying deep learning—largely rely on synaptic connectivity to sustain activity.

Beyond cellular mechanisms, the specific functional contribution of the hippocampus to spatial working memory remains a subject of intense debate. It has long been contested whether the hippocampus supports spatial working memory by maintaining task-specific content (working memory hypothesis) or by supplying an ongoing spatial representation (cognitive map theory) (*33*, *34*). While human studies repeatedly indicate that hippocampal persistent firing encodes working memory content (*8*), decoding analyses from the rodent hippocampus have shown an absence of working memory content (e.g., left versus right turns) during the delay period (*13*, *35*, *36*). Thus, the information represented by hippocampal persistent firing during spatial working memory still remains unclear. Notably, both working memory maintenance and spatial representation have been modeled using similar attractor-based dynamics (*37*, *38*), indicating that the maintenance of head direction or spatial information is associated with persistent firing (*39*, *40*). However, whether the maintenance of spatial representations in vivo relies on network-level connectivity or individual cellular mechanisms remains to be determined.

Here, we test the contribution of intrinsically generated persistent firing to the maintenance of internal representations in vivo and

[1]Leibniz Institute for Neurobiology, Brenneckestraße 6, 39118 Magdeburg, Germany. [2]Cognitive Neurophysiology Group, German Center for Neurodegenerative Diseases (DZNE), 39120 Magdeburg, Germany. [3]Institute of Physiology, Medical Faculty, Otto-Von-Guericke University, 39120 Magdeburg, Germany. [4]Molecular Neuroplasticity Group, German Center for Neurodegenerative Diseases (DZNE), 39120 Magdeburg, Germany. [5]Medical Faculty, Otto-von-Guericke University (OVGU), 39120 Magdeburg, Germany. [6]Center for Behavioral Brain Sciences (CBBS), 39106 Magdeburg, Germany.
*Corresponding author. Email: motoharu.yoshida@lin-magdeburg.de
†Present address: Gene Therapy Consultancy, Ackerstr. 34, 39112 Magdeburg, Germany.

to cognitive performance. We first identify the TRPC4 ion channel as a molecular mechanism underlying intrinsic persistent firing and subsequently examine neural activity in mice during a spatial working memory task under TRPC4 knockdown (KD). Persistent firing observed in control animals during the delay period of the task was markedly reduced in TRPC4 KD mice, indicating that intrinsic cellular mechanisms support persistent firing in vivo. Notably, the transient activity of cells before and after the delay period was not altered, highlighting the specific role of TRPC4 channels in sustained firing. Spatial working memory performance was significantly impaired, providing the evidence for a functional role of hippocampal persistent firing in this task. Using support vector machine (SVM) decoding and spatial information measurements, we reveal that hippocampal persistent firing reflects the sustained activity of place cells with high spatial information when animals remain at fixed locations (the start and goal areas) for extended periods. Furthermore, using Bayesian decoding and SVM-based classification, we demonstrate that spatial representation errors increased rapidly and that left-right goal prediction deteriorated upon entry into the goal areas in TRPC4 KD mice, indicating impaired maintenance of spatial representations. Notably, the strength of persistent firing at the goal locations correlated with task performance. These data suggest that hippocampal persistent activity supports spatial working memory by maintaining instantaneous spatial representations of the left versus right goals for the encoding of the corresponding trial types during a sample phase, which can then be used to guide spatial memory behavior during the subsequent choice phase. These results, together with previous studies on intrinsic persistent firing, position individual neurons as active units of information retention, extending their traditional role as passive input-output units and adding unexplored dimensions to our understanding of memory and neural computation.

RESULTS

TRPC4 KD suppresses intrinsic persistent firing in vitro

We developed a short hairpin RNA (shRNA) TRPC4 channel KD (TRPC4 KD) virus and a control virus with a scrambled sequence (Scrambled) to test the role of intrinsic persistent firing in vivo [see Materials and Methods and Fig. 1A; one-way analysis of variance (ANOVA), $P < 0.01$; Tukey post hoc test corrected for multiple comparison, no virus versus Scrambled: $P = 0.33$, no virus versus TRPC4 KD: $P < 0.05$, and Scrambled versus TRPC4 KD: $P < 0.01$; $n = 5$ in all groups] (*41*). The mice received bilateral injections of either virus into the CA1 region (Fig. 1B). First, a loss of intrinsic persistent firing was confirmed using in vitro patch-clamp recordings of hippocampal CA1 cells in the presence of the cholinergic receptor agonist carbachol (10 μM; Fig. 1C) (*20*, *25*). Percentages of cells responded with persistent firing (Fig. 1D; Fisher's exact test, noninjected versus Scrambled: $P = 1$; noninjected versus TRPC4 KD: $P = 0.0079$; Scrambled versus TRPC4 KD: $P = 0.0063$; $n = 12$, 14, and 14, respectively), the frequency of persistent firing (Fig. 1E; Kruskal Wallis test, $P = 0.0023$, $\chi^2 = 12.18$, df = 2; Tukey post hoc test, noninjected versus Scrambled: $P = 0.99$, noninjected versus TRPC4 KD: $P = 0.0077$, and Scrambled versus TRPC4 KD: $P = 0.0074$), and membrane depolarization (Fig. 1F; Kruskal-Wallis test, $P = 0.0116$, $\chi^2 = 8.92$, df = 2; Tukey post hoc test, noninjected versus Scrambled: $P = 0.89$, noninjected versus TRPC4 KD: $P = 0.017$, Scrambled versus TRPC4 KD: $P = 0.047$; $n = 12$, 14, and 14) were significantly lower in the TRPC4 KD group than in the two control groups. Basic properties of TRPC4 KD cells—such as the resting membrane potential, input resistance, adaptation index, and intrinsic excitability—did not significantly differ from those in the control groups (except for intrinsic excitability measured with 100 pA current injection, Kruskal-Wallis test, $P = 0.0193$, $\chi^2 = 7.89$, df = 2; Table 1). In summary, TRPC4 KD significantly decreased the ability of individual cells to support persistent firing while preserving basic cellular properties.

TRPC4 KD impairs spatial working memory

Second, the effect of TRPC4 KD on spatial working memory was assessed by a delayed nonmatch-to-sample paradigm using an automated T-maze (Fig. 1, G to I, and fig. S1). The scrambled control group mice consistently performed ~80% correctly from day two. On the other hand, the performance of the TRPC4 KD group remained ~60% correct over the 10 days of testing (Fig. 1J; two-way ANOVA, main effect of animal group, $P < 0.0001$; post hoc t tests with multiple comparison correction: day 3: $P = 0.020$, day 4: $P = 0.0086$, day 6: $P = 0.0019$, day 8: $P < 0.001$, and day 10: $P = 0.0040$). Group comparisons demonstrated that hippocampal TRPC4 KD significantly impaired working memory performance compared to scrambled control mice (Fig. 1K; t test, $P < 0.001$; $n = 13$ and 14 for control and KD groups, respectively). These results indicate that TRPC4 channels in CA1 neurons are necessary for spatial working memory.

TRPC4 KD suppresses in vivo persistent firing

Classical theory and evidence suggest that persistent firing supports memory maintenance (*8*, *33*, *42*). We tested whether TRPC4 KD affected persistent firing in the T-maze using in vivo recordings. We observed cells with increasing firing rates during the delay (maintenance) period (0 to 30 s; orange line, Fig. 2A). To quantify this increased firing, we calculated the z-scored firing rate of individual cells around the delay period using the predelay period as the baseline in cells from the control and TRPC4 KD groups (Fig. 2B and see Materials and Methods). The cells were sorted on the basis of their mean activity during the delay period (0 to 25 s; orange line at the top of Fig. 2B). While a substantial portion of cells at the top of the figure showed increased activity during the delay in the control group (top, ~10%; Fig. 2B, left), such an increase was less prominent in the TRPC4 KD group (Fig. 2B, right). The distribution of the mean activity during the delay period for all recorded cells was narrower in the TRPC4 KD group than in the control group, as quantified by the interdecile (10th to 90th percentile) and interquartile ranges (fig. S2A caption). In addition, the variance of this distribution was significantly smaller in the KD group (fig. S2A caption), suggesting an attenuated modulation (both increases and decreases) of firing rates in the TRPC4 KD group.

In agreement with this, the activity of the top 10% most active cells was significantly lower in the TRPC4 KD group [top panels in Fig. 2, C and D; Wilcoxon rank-sum (WRS) test, $P < 0.001$]. Similarly, the suppression of the bottom 10% cells in the TRPC4 KD group was significantly weaker (bottom panels in Fig. 2, C and D; WRS test, $P < 0.001$). Accordingly, TRPC4 KD significantly reduced the number of delay-activated (Act) and delay-suppressed (Sup) cells and increased the number of nonmodulated (NM) cells (see Materials and Methods for the definition; Fig. 2E; χ^2, $P < 0.001$ for all categories). Moreover, the degree of activation within the Act cells and the degree of suppression within the Sup cells were significantly smaller in the KD group than in the control group (fig. S2, B to D), indicating

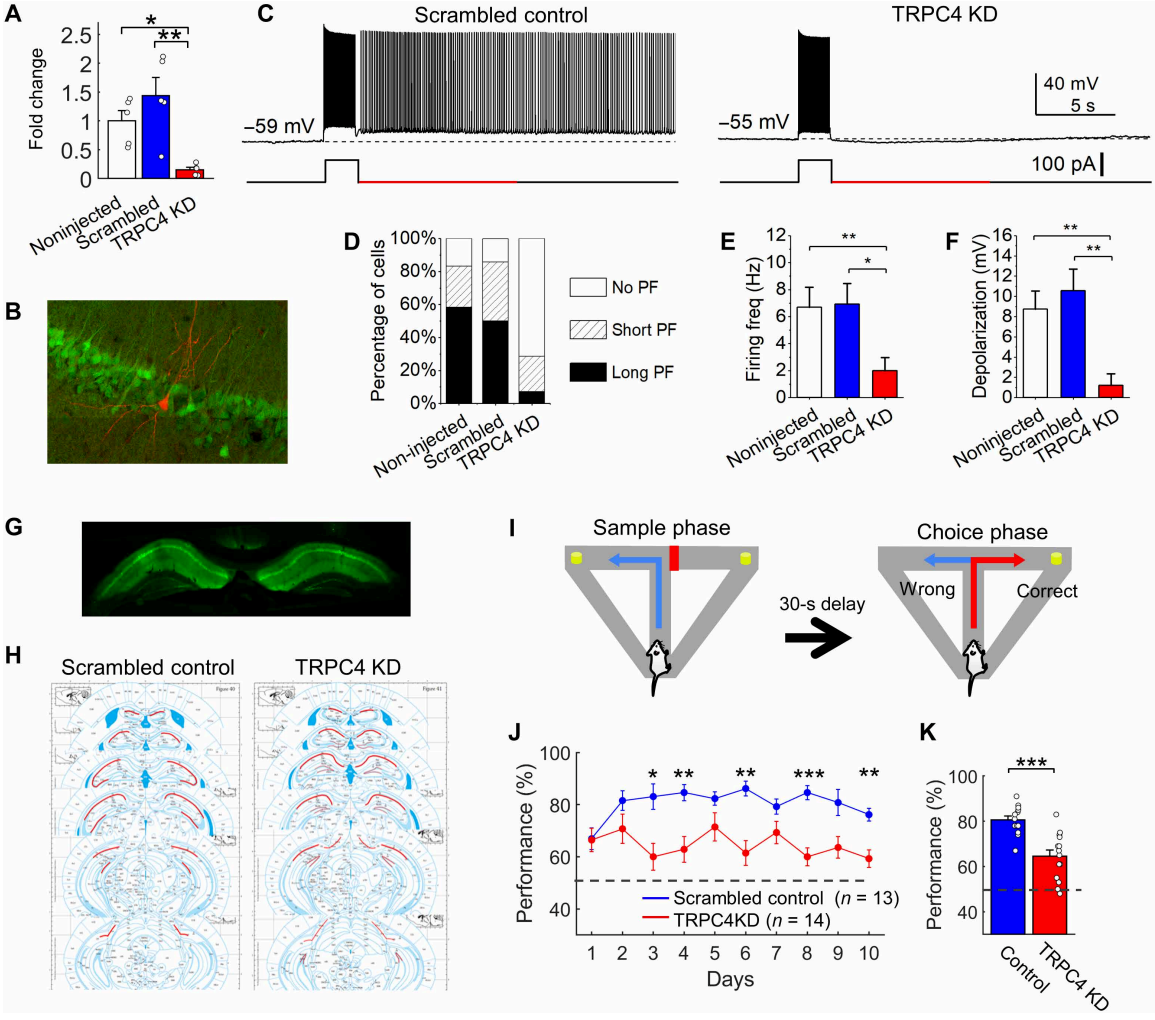


Fig. 1. Hippocampal TRPC4 KD significantly reduces intrinsic persistent firing and impairs the delayed nonmatch-to-sample spatial working memory task. (**A**) Reduced TRPC4 mRNA expression by the TRPC4 KD virus confirmed by reverse transcription quantitative polymerase chain reaction (one-way ANOVA, $P < 0.01$; Tukey post hoc test corrected for multiple comparison, no virus versus Scrambled: $P = 0.33$, no virus versus TRPC4 KD: $P < 0.05$, Scrambled versus TRPC4 KD: $P < 0.01$; $n = 5$ in all groups). (**B**) An example hippocampal slice with green fluorescent protein (GFP)–expressing cells due to TRPC4 KD virus injection and a recorded neuron (red). (**C**) Persistent firing observed in a CA1 pyramidal cell infected with the scramble control virus (upper trace) and an absence of persistent firing in a cell infected with the TRPC4 KD virus (lower trace). The bottom trace indicates injected current. The red part of this trace corresponds to the 10 s interval when firing rate and depolarization were measured in (E) and (F). (**D**) Percentages of cells that responded with persistent firing (No PF: no persistent firing. Short PF: persistent firing which did not last for 30 s. Long PF: persistent firing lasted longer than 30 s). (**E** and **F**) TRPC4 KD significantly decreased frequency of persistent firing and membrane depolarization measured during the 10 s period after the triggering stimulus. KD, knockdown; ANOVA, analysis of variance. (**G**) An example of hippocampal GFP expression after TRPC4 KD virus injection. (**H**) Summary of virus expression along the rostro-caudal axis from all mice. Red lines indicate the maximum extent of virus spread in each rostro-caudal plane. (**I**) Delayed nonmatch-to-sample spatial working memory task in a T-maze. (**J**) Working memory performance in scrambled control and TRPC4 KD group animals over 10 days. (**K**) Averaged working memory performances of TRPC4 KD mice were significantly lower than the scrambled control group.

Table 1. Comparisons of passive membrane properties. RMP, resting membrane potential; resistance, input resistance; adaptation index, firing rate adaptation index. Asterisk (*) indicates significant differences between groups ($P < 0.05$, Kruskal-Wallis test).

	RMP (mV)	Resistance (MΩ)	Adaptation index	Intrinsic excitability (Hz)			
				50 pA	100 pA	150 pA	200 pA
Noninjected	−64.19 ± 0.18	163.31 ± 4.82	0.43 ± 0.02	5.09 ± 0.48	20.45 ± 0.69	29.55 ± 0.71	39 ± 0.54
Scrambled	−64.20 ± 0.21	180.66 ± 2.72	0.53 ± 0.02	2.5 ± 0.35	13.71 ± 0.56	25.21 ± 0.64	33.21 ± 0.82
TRPC4 KD	−63.79 ± 0.25	173.85 ± 2.62	0.67 ± 0.03	7.86 ± 0.49	*22.71 ± 0.59	30.5 ± 0.70	36.57 ± 0.65

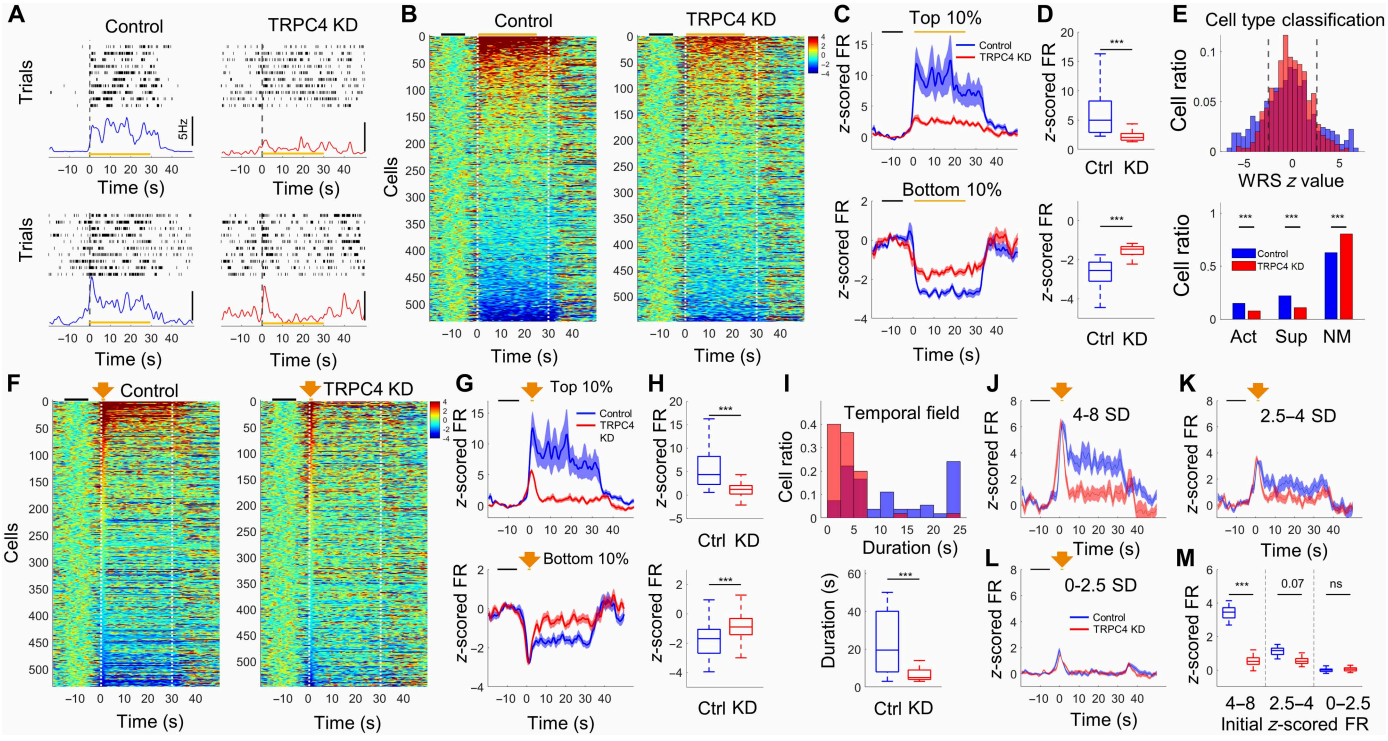


Fig. 2. TRPC4 KD suppresses in vivo persistent activity. (**A**) Example firing pattern (raster plot) and averaged firing rate (bottom) of two cells from the control and TRPC4 KD groups around the delay period of the spatial working memory task. Scale bars, 5 Hz. (**B**) *z*-scored firing rate of all cells sorted by the delay period activity. Vertical dashed lines indicate the onset and offset of the delay period. Black and orange horizontal lines at the top of each panel indicate the baseline period and period for cell sorting, respectively. (**C**) Averaged *z*-scored firing rate (FR) of the top (top) and bottom (bottom) 10% cells in (B). (**D**) Comparison of *z*-scored firing rate of the top (top) and bottom (bottom) 10% cells in (B) averaged over the delay period (0 to 25 s). (**E**) Classification of activated (Act), suppressed (Sup), and nonmodulated (NM) cells using the WRS test. The top shows the distribution of WRS *z* values, and the bottom shows the ratio of cells in each category. (**F**) *z*-scored firing rate of all cells sorted by the activity at the initial part of the delay period (0 to 2 s). Black and orange horizontal lines (indicated by orange arrows) at the top of each panel indicate the baseline period and period for cell sorting, respectively. (**G**) Averaged *z*-scored firing rate of top (top) and bottom (bottom) 10% cells in (F). (**H**) Comparison of *z*-scored firing rate of the top (top) and bottom (bottom) 10% cells in (F) averaged over the delay period (0 to 25 s). (**I**) Distribution (top) and comparison (bottom) of temporal field duration among the top 10% cells. (**J** to **L**) Averaged *z*-scored firing rate of cells that showed 4 to 8 (J), 2.5 to 4 (K), and 0 to 2.5 (L) SD peak *z*-scored firing rate at the initial part of the delay (0 to 2 s). (**M**) Comparison of activity during the delay (4 to 25 s) period in cells that showed different levels of initial activation corresponding to (J) to (L).

that TRPC4 KD reduced both the number of modulated cells and the intensity of modulation within these populations.

If intrinsic persistent firing was supporting in vivo persistent firing, then TRPC4 KD should increase transiently active cells. To test this, we sorted the cells using only activity during the first 2 s of the delay period (0 to 2 s; Fig. 2F). The activity of initially active cells significantly decreased during the delay period in the KD group, whereas more cells in the control group maintained their activity until the end of the delay period (Fig. 2, F and G). The activity measured during the entire delay period (0 to 25 s) was significantly lower in the KD group (Fig. 2H; WRS test, $P < 0.001$ and $P < 0.001$ for top and bottom panels, respectively). We measured the temporal field duration to quantify the duration of continuous elevation of the firing rate (Fig. 2I and see Materials and Methods). While the control group showed a wide distribution of temporal field duration up to the full delay duration, most of the TRPC4 KD group cells showed a temporal field shorter than 7.5 s (Fig. 2I, top). The mean temporal field duration was significantly shorter in the TRPC4 KD group (Fig. 2I, bottom; WRS test, $P < 0.001$). These data indicated that TRPC4 KD increased transient firing and decreased persistent firing in vivo, as expected from our in vitro results.

However, the initial activity of the top 10% cells was stronger in the control group (Fig. 2G, top), which could have resulted in stronger persistent firing in this group. To test this possibility, we filtered cells based on their initial (0 to 2 s) activity levels (Fig. 2, J to M). The control group cells with initial activity increases of 4 to 8 and 2.5 to 4 SDs maintained a greater elevated level of activity until the end of delay compared to KD group cells (Fig. 2, J and K), whereas those with initial activity of 0 to 2.5 SD did not show elevated activity (Fig. 2L). The sustained activity measured at 4 to 25 s was smaller in the KD group with 4 to 8 and 2.5 to 4 initial SDs (Fig. 2M; WRS test, $P < 0.001$, $P = 0.07$, and $P = 0.58$ for 4 to 8, 2.5 to 4, and 0 to 2.5 initial SDs, respectively), indicating that the different activities between the two groups are not simply due to the difference in initial activation. Thus, more KD cells showed transient activity during the delay period, supporting the contribution of TRPC4 channels to sustained activity in vivo in a similar manner as in vitro.

Temporal sorting reveals reduced persistent firing in TRPC4 KD mice

We further characterized the effect of TRPC4 KD using temporal sorting (*11*, *12*). For this analysis, we selected putative pyramidal

cells active (firing rate > 2 Hz) in at least one bin during or near the delay period (see Materials and Methods, 196 of the 533 control cells and 235 of the 549 TRPC4 KD cells) and sorted them according to their activity peak time, as in previous reports (Fig. 3A) (*11*). We found an overrepresentation of the initial part of the delay period (0 to 3 s) in both the control and TRPC4 KD group (Fig. 3B). However, TRPC4 KD did not significantly alter peak time distribution (WRS test, $P = 0.74$).

To evaluate potential effects of TRPC4 KD on cells with different peak times, cells were separated into three groups based on their peak times during the delay (Fig. 3A). While cells that peaked at 0 to 2.5 s (group 1) showed transient peak activity, the other two groups that peaked later in the delay (2.5 to 16.5 s: group 2; 16.5 to 30 s: group 3) exhibited, on average, an elevated firing rate throughout the delay period in the control group (Fig. 3C, left). Please note that these group 1 cells do not represent the exact same population as the top 10% cells in Fig. 2 (F to H). While cells that were active at the beginning of the delay period and then subsequently exhibited even more robust activation toward the middle or end of the delay period (due to persistent firing) were included in the top 10% cohort in Fig. 2 (F to H), these cells were classified here as group 2 or 3. The exclusion of these robustly persistent cells from group 1 consequently results in a less elevated average firing rate for this cluster.

While TRPC4 KD did not affect the transient activation of cells at the initial part of the delay (group 1), it reduced long-lasting elevated firing of group 2 and group 3 cells (Fig. 3C, right). Accordingly, the firing rate averaged over the delay period was significantly lower in groups 2 and 3 of the KD group but not in group 1 (Fig. 3D). Combining all cells that peaked during the delay, the KD group had more cells with shorter fields (see Materials and Methods and Fig. 3E; WRS test, $P < 0.001$). The duration of the field from the KD group cells was significantly shorter in groups 2 and 3 (Fig. 3F; WRS test, $P = 0.32$, $P < 0.001$, and $P = 0.006$ for groups 1, 2, and 3, respectively). The specific effect of TRPC4 KD on cells with longer temporal fields,

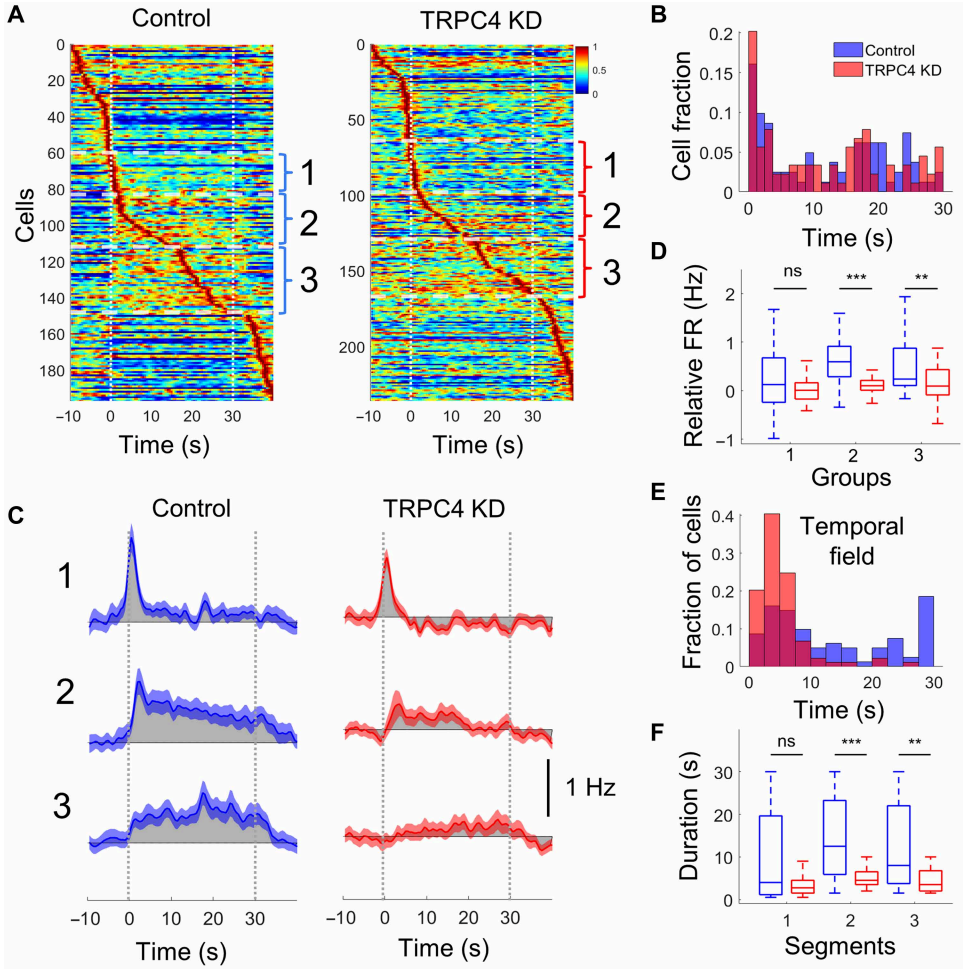


Fig. 3. Peak time sorting also shows reduced persistent activity in TRPC4 KD mice. (**A**) Normalized firing rate of cells sorted by their peak times. Vertical dashed lines indicate the onset and offset of the delay period. Horizontal dashed lines and numbers (*1–3*) on the right of each panel indicate divisions of cells by their peak times (group 1: 0 to 2.5 s, group 2: 2.5 to 16.5 s, and group 3: 16.5 to 30 s). (**B**) Distribution of peak time of all cells within the delay period. Peak time distribution is not significantly affected by TRPC4 KD. (**C**) Averaged relative firing rate (compared to baseline firing rate) of cells belonging to each peak time segment shown in (A). Gray shades indicate a difference from the baseline firing rate. Note a prominent, long-lasting elevated firing rate in control cells in groups 2 and 3. (**D**) Relative firing rate (FR) measured during the delay (0 to 30 s) compared to the baseline period in cells in each peak time segment. (**E**) Distribution of temporal field duration of all cells peaked during the delay period (groups 1 to 3). (**F**) Comparison of the duration of the field in each group.

further support the idea that the ability of single neurons to sustain firing is necessary specifically for persistent firing in vivo.

Activity outside the delay period is intact

To further assess whether the effect of TRPC4 KD was specific to the delay period, we compared the activity of cells at different time points, ranging from 4 s before delay onset to 3 s after the delay (Fig. 4). First, cells were sorted using the *z*-scored activity of each cell at 3 to 4 s before the start of the delay period (−4 to −3 s; Fig. 4A), and the average activity of the top 10% cells from the control and KD groups was compared (Fig. 4D, most left). These cells were only temporarily active and did not display persistent firing in either group, indicating that persistent firing was not ubiquitous. The activity of the top 10% most active cells during this 1-s window was not different between the control and KD groups (−4 s in Fig. 4E), indicating that TRPC4 KD did not have a strong effect before the delay. Similar results were obtained 2 s before delay onset (−2 to −1 s; Fig. 4D, second from left; time, −2 s in Fig. 4E). In contrast, control group cells activated during the delay (0 to 1, 10 to 11, and 20 to 21 s) showed stronger activity than KD cells during these 1 s windows [Fig. 4, B and D (middle three panels); time: 0, 10, and 20 s in Fig. 4E]. Last, when active cells were detected after the delay period [1 to 2 and 3 to 4 s later; Fig. 4, C and D (two rightmost panel)], the activity of these cells was transient and similar between the two groups (time: 1 and 3 s in Fig. 4E).

To validate the observation in Fig. 4D that cell populations active either preceding or following the delay period were not strongly active during the delay period, we tracked their activity specifically during the delay (Fig. 4F). For example, after identifying the top 10% most active cells within the −4- to −3-s window (the leftmost panel of Fig. 4D), the activity of this cohort of cells was measured during the delay period (green line in the same panel). This value

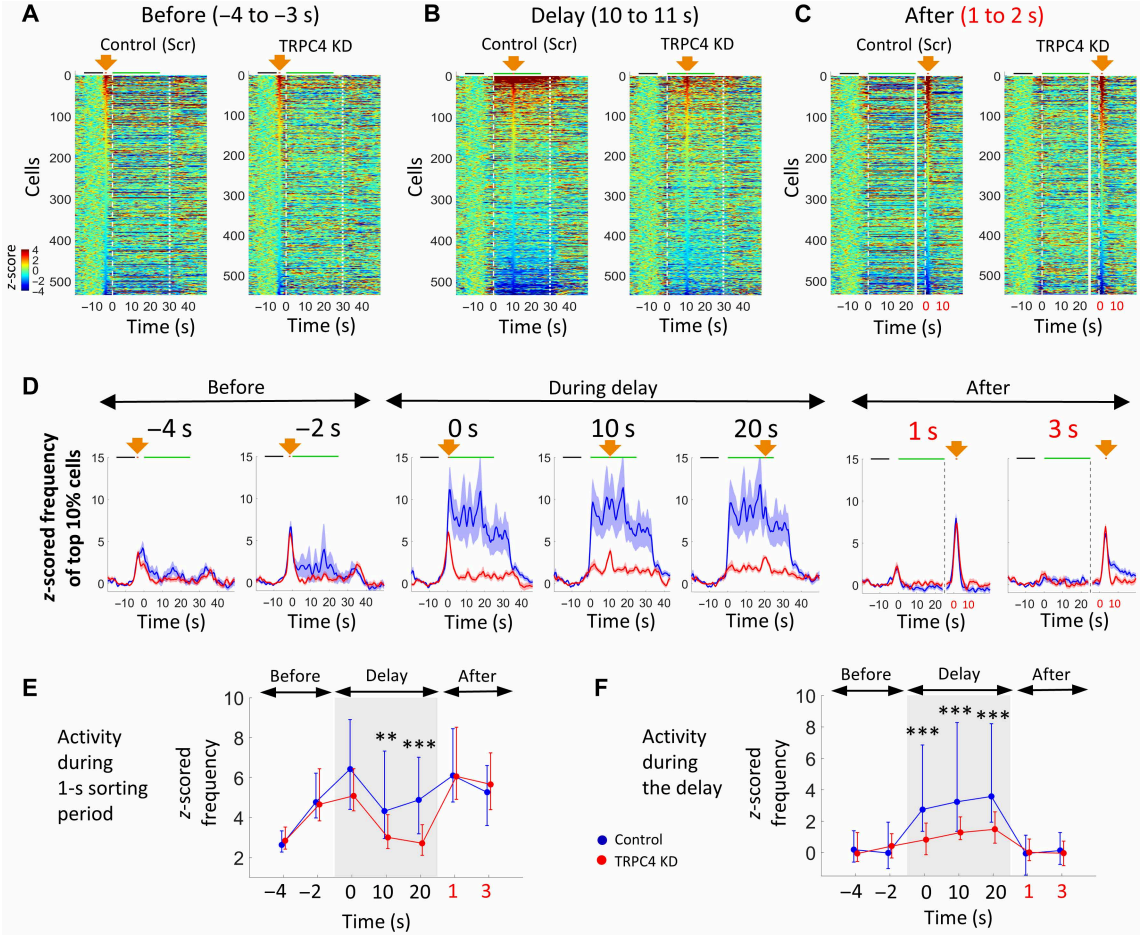


Fig. 4. Activity outside the delay period is not strongly affected by TRPC4 KD. (**A** to **C**) *z*-scored firing rate of all cells sorted by their activity during the (A) 4 to 3 s before delay, (B) 10 to 11 s from the start of delay, and (C) 1 to 2 s after the delay offset. Vertical dashed lines indicate the onset and offset of the delay period. Black, orange (indicated by orange arrows), and green horizontal lines at the top of each panel indicate the baseline period, period for cell sorting, and period for delay activity measurement, respectively. In (C), the white solid vertical line indicates the separation of the color plot into two parts that are aligned to the delay onset (left of the line) and offset (right of the line). (**D**) Averaged *z*-scored firing rate of the top 10% cells at different time points. Note that the cells chosen for each panel are therefore different. The vertical dotted lines in the two last panels correspond to the time when data alignment changed as in (C). (**E**) Comparison of *z*-scored firing rate of the top 10% cells measured specifically during the 1-s-long sorting period [corresponding to the orange horizontal lines with arrows in (D); rank sum test with Bonferroni correction, $P = 0.31$, $= 1.45$, $= 0.29$, $= 0.003$, < 0.001, $= 1.45$, and $= 0.28$, respectively]. (**F**) Comparison of *z*-scored firing rate of the top 10% cells measured specifically during the delay period [corresponding to the green horizontal lines in (D); rank sum test with Bonferroni correction, $P = 0.88$, $= 1.46$, < 0.001, < 0.001, < 0.001, $= 1.47$, and $= 1.10$, respectively]. Data points show the median, and error bars indicate the upper and lower quartiles.

was plotted at the −4-s time point in Fig. 4F, and this procedure was repeated for the active cell populations defined at each subsequent time point. These results confirm that cells strongly active outside of the delay period do not contribute to persistent firing during the delay period in either the control or TRPC4 KD group. Together, these suggest that persistent firing does not occur before or after the delay period and that TRPC4 KD specifically affects the activity of neurons during the delay period, as opposed to worsening the signal-to-noise ratio throughout the task.

Activity of putative pyramidal cells and interneurons

We next investigated whether the difference in the delay period activity between control and TRPC4 KD mice was cell type–dependent. We separated recorded neurons into putative pyramidal neurons and interneurons based on their average firing rates and spike durations (see Materials and Methods). Putative pyramidal cells in the control group showed strong activity during the delay, with TRPC4 KD suppressing this activity (fig. S3, A to D). On the other hand, the activity of the top 10% putative interneurons during the delay period did not differ between the control and TRPC4 KD groups (fig. S3, E to H). This suggests that putative interneurons are not the main source of the observed TRPC4 KD-dependent changes.

Information coded by persistent firing

Next, we investigated the nature of information coded by cells with strong persistent firing during the delay period. The hippocampus may support spatial working memory in at least two ways. First, persistent firing may sustain working memory content (e.g., turn direction in the sample trial) during the delay period (*33*, *42*). Second, the hippocampus may support spatial working memory tasks by encoding information about the current spatial location (*34*, *43*). For example, when a mouse is at one of the goal locations during the sample phase, an accurate representation of the left versus right goals could be essential for the accurate encoding of the left versus right sample trial types in memory (e.g., as a form of synaptic potentiation), which in turn supports the subsequent arm choice in the choice phase. However, whether the hippocampal long-lasting persistent firing codes for the turn direction or current spatial information remains unclear. In addition, it remains unknown whether this persistent firing is observed outside the delay period in this task.

We first compared the activity of cells in the control group during the delay period with that during the intertrial interval (ITI; Fig. 5A). Since the animals were in the same start area in both the delay period and ITI, the different activities in these phases may suggest the coding of task-relevant information. Cells were sorted according to their activity during the delay period (Fig. 5B). Baseline and sorting period were the same as in Fig. 2B. Control cells highly active during the delay period were strongly active during ITI as well, without significant difference, as shown in Fig. 5 (B and C) (WRS test, $P = 0.40$). The activity of individual cells during the delay period was similar to that during ITI, as shown in Fig. 5D.

We further used an SVM to test whether it could be trained to predict the delay and ITI phases based on the activity of all cells in each recording session (control: $n = 16$ and TRPC4 KD: $n = 18$ sessions; see Materials and Methods for details and Fig. 5, E and F). SVM could not differentiate the delay versus ITI phases in any of the recordings (z values were lower than 1.96) from the control and TRPC KD groups. Furthermore, there were no differences between the control and KD groups (WRS test, $P = 0.61$ and $P = 0.59$ for Fig. 5, E and F, respectively). Together, these findings contradicted the idea that persistent firing codes for task phase–relevant information.

Second, we asked whether the direction of the past or future turns was coded in persistent activity observed during the delay period. We sorted cells from the control group using the delay activity of the left trials (left turn on the sample trial; Fig. 5G, left) and used the same order for the delay activity of the right trials (Fig. 5G, right). A small but significant difference was observed when comparing the activity of the top 10% cells (Fig. 5H; WRS test, $P = 0.0058$). The activity of individual cells in the left and right delay periods was generally similar but showed more differences than the comparison between the ITI and delay phases (Fig. 5I). While this difference between the left and right delay activity indicates the potential existence of coding of the turn direction, random noise may result in these differences.

Therefore, we further used an SVM to test whether the population activity codes for the left versus right turn in each recording session (control, $n = 15$; TRPC4 KD, $n = 14$). SVM prediction accuracy exceeded 70% in most of the sessions (Fig. 5J) just before the onset of the delay period (−3 to 0 s), when the animal was still in the return arm of the T-maze, and this prediction accuracy was significantly higher than the chance level in approximately half (53.3%) of the sessions (Fig. 5K). However, prediction performance decreased quickly as the delay started (0 to 3 s; Fig. 5, J and K), and almost none of the sessions reached a significant level in either the control or TRPC KD group after 3 s (3 to 25 s) in the delay period. No difference was observed between the SVM performance of the control and KD groups for any of the three time segments (WRS test, $P =$ 0.49, 0.91, and 1, respectively, in Fig. 5J; $P = 0.20$, 0.28, and 0.98, respectively, in Fig. 5K).

We further asked whether the delay period activity codes for the future turn direction (prospective coding) rather than the past turn direction from the sample phase (retrospective coding). The SVM prediction for prospective coding was tested using the activity from the 3- to 25-s period during the delay of all or only correct trials (Fig. 5, L and M). Most of the session did not reach significant levels both in the control and KD group, and there was no difference between the control and KD (WRS test, $P = 0.98$ and $P = 0.59$, respectively, in Fig. 5L; WRS test, $P = 0.78$ and $P = 0.52$, respectively, in Fig. 5M). Together, these suggest that coding for the direction of turns during the delay period is weak. These agree with recent publications which pointed out that hippocampal delay period activity does not (*35*, *36*) or only weakly (*44*) codes for the direction of the past or future turns.

Persistently active cells encode spatial information

Next, we tested the hypothesis that persistently active cells primarily code for spatial information. Computational models of hippocampal place cells suggest that spatial representation is maintained by the self-sustained activity of a subset of place cells (*40*); therefore, persistent firing might be involved in the maintenance of spatial representation. We first sorted cells in order of the strength of persistent firing during the delay period as in the previous sections (Fig. 6A). We then calculated the spatial information of each cell using the entire duration of the recording, including the sample and choice phases from all 10 trials (Fig. 6B). Spatial information was particularly high in the control group cells that showed strong persistent firing (blue line, Fig. 6B). Spatial information of the top 10% cells in Fig. 6A was significantly lower in the KD group compared to

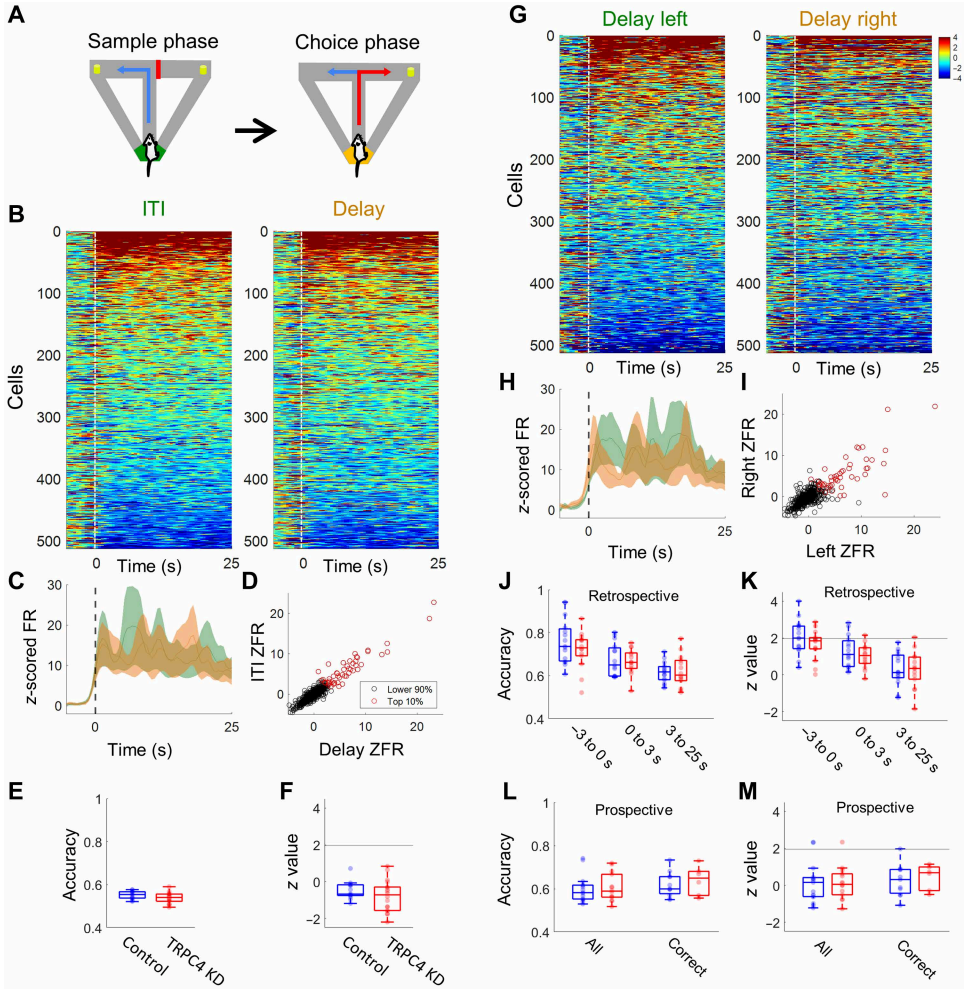


Fig. 5. Persistently firing cells do not strongly code task phases and direction of turn. (**A**) ITI (green) in the sample phase and delay period (orange) in the choice phase. (**B**) *z*-scored firing rate of all cells sorted by the averaged activity during the ITI (0 to 25 s) in both ITI and delay. Vertical dashed lines indicate the onset of ITI or the delay period. (**C**) Averaged activity of the top 10% cells in B from ITI (green) and delay period (orange). (**D**) Comparison of activity during ITI and the delay period from all cells. Each circle corresponds to a cell. The top 10% cells (based on common sorting) are indicated by red circles. (**E** and **F**) Accuracy and *z* value from the SVM prediction of ITI versus delay phase based on the activity of all cells. The horizontal line in (F) indicates a 5% significance level. (**G**) *z*-scored firing rate of all cells around the delay period in the left and right trials (defined by the turn at the sample phase: retrospective coding), sorted by the average activity of the left trials. (**H**) Averaged activity of the top 10% cells in (G) from the left (green) and right (orange) trials. (**I**) Comparison of activity from left and right trials for all cells. Each circle corresponds to a cell. The top 10% cells (based on common sorting) are indicated by the red circles. (**J** and **K**) Accuracy and *z* value from the SVM prediction of left versus right trials based on the activity of all cells at different segments before (−3 to 0) and during (0 to 3 s, 3 to 25 s) the delay period. (**L** and **M**) Accuracy and *z* value from the SVM prediction of future left versus right trials during (3 to 25 s) the delay period (prospective coding). SVM, support vector machine.

the control group (Fig. 6C; WRS test, $P = 0.0024$; $n = 53$), whereas that of the bottom 10% cells was significantly higher in the KD group (Fig. 6D; WRS test, $P < 0.001$; $n = 55$).

We visualized the spatial rate maps of the top 10% cells in control and TRPC4 KD groups (Fig. 6, E and F). While the control group cells generally showed a clear field within the start area, fields of TRPC4 KD cells were less confined, often having multiple fields outside the start area (Fig. 6, E and F). The averaged rate map from top 10% control cells showed a distinct firing at the start area, while that from the KD cells showed spatially less defined activity (Fig. 6, G and H). This suggests that cells with strong persistent firing during the delay period are those with better-defined place fields in the start area and consequently have higher spatial information. This suggests that TRPC4 KD destabilized spatial representation by preventing persistent activity of CA1 place cells while the animal remained in the start area.

Selective decrease of spatial information in start and goal areas

In the T-maze task, in addition to the start area, the animals stayed for an extended period in the goal areas where they consumed their rewards, whereas they run through other subareas of the maze (e.g., stem and return arm). If intrinsic persistent firing supports continuous place cell activity, then TRPC4 KD might have affected spatial representation specifically in the start and goal areas without affecting that in other subareas. To test this, we first detected the location

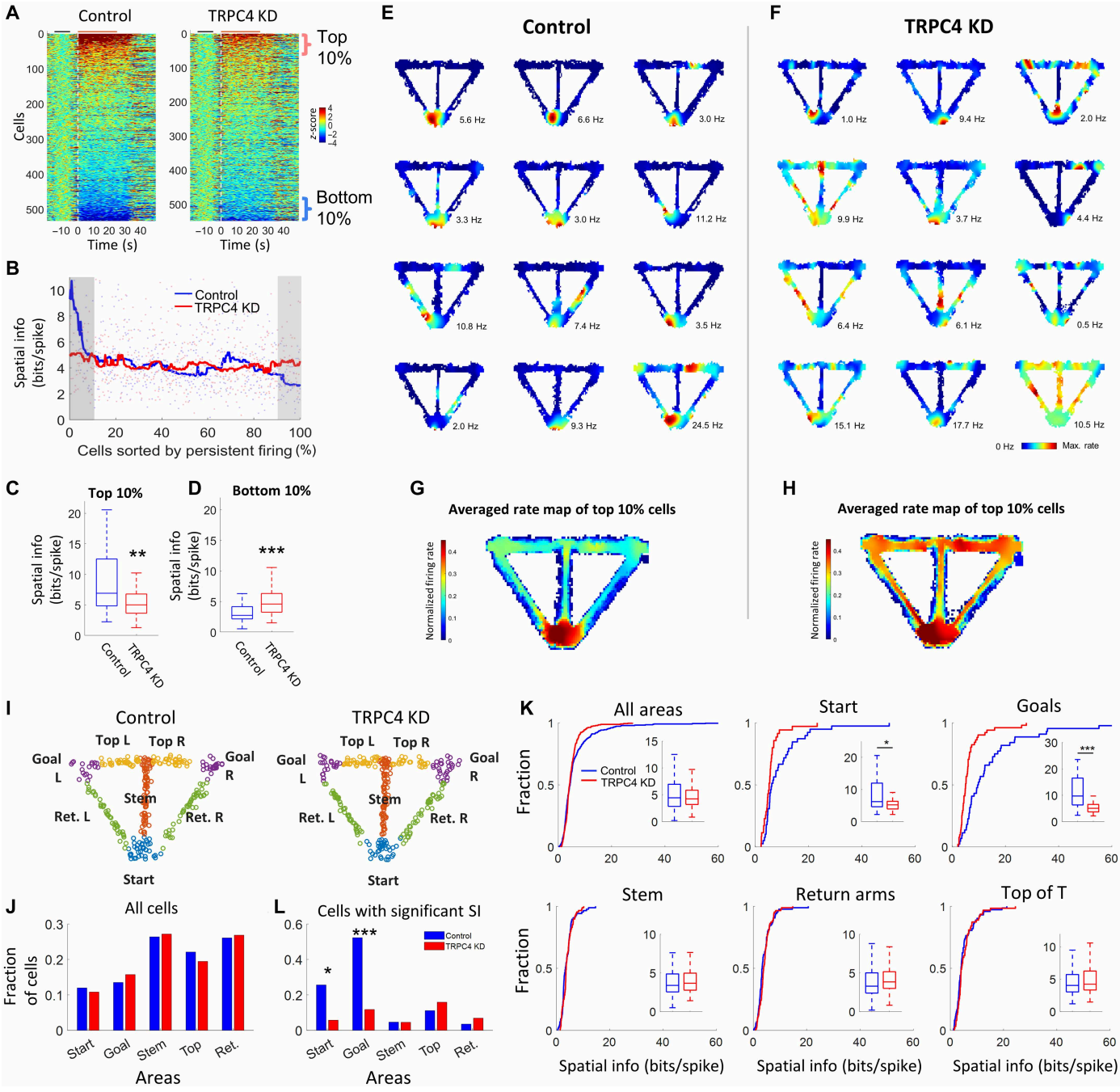


Fig. 6. TRPC4 supports persistent activity of spatial cells when animals stay in a place for an extended duration. (**A**) *z*-scored firing rate of all cells sorted by the averaged activity during the delay period (0 to 25 s), as in Fig. 2B. Vertical dashed lines indicate the onset of the delay period. (**B**) Spatial information of all cells plotted in the order of the sorting in (A). Solid lines indicate the moving average. Grey shaded areas indicate the top and bottom 10% cells. (**C** and **D**) Comparison of spatial information between the control and TRPC4 KD groups in the top and bottom 10% cells. (**E** and **F**) Example spatial rate maps of the top 10% cells in control (E) and TRPC4 KD (F) groups. The maximum firing rate of each cell is indicated at the bottom right corner of each panel. (**G** and **H**) Averaged spatial rate maps of all top 10% cells in the control (G) and TRPC4 KD (F) groups. (**I**) Distribution of peak firing location of all putative pyramidal cells on the T-maze. Each circle corresponds to a cell, and colors indicate different subareas. Top, top of the T-maze; Ret., return arm; L, left; R, right. (**J**) Fractions of cells classified into each subarea. (**K**) Distribution of spatial information of cells in all and each subarea. Insets are comparisons of spatial information between the control and KD cells. (**L**) Number of place cells with significant spatial information in each subarea.

of firing fields within the T-maze for each putative pyramidal cell (see Materials and Methods). Next, we divided cells into different groups depending on the subareas of the T-maze where the location of field centers fell (Fig. 6I). The number of cells in each subarea was similar in the control and KD groups (Fig. 6J).

We then compared the spatial information of the cells in each subarea (Fig. 6K). Spatial information was slightly smaller in the TRPC4 KD group when all subareas were combined (all areas; WRS test, $P = 0.56$), without a significant difference. Consistent with previous observations, the spatial information of the cells in the start area was significantly lower in the KD group; WRS test, $P = 0.019$). A similar difference was observed in the goal area, where the animals stayed for an extended time (WRS test, $P < 0.001$). However, spatial information was not significantly different in other areas, such as the stem, return arms, and top of the T (WRS test, $P = 0.41$, $P = 0.19$, and $P = 0.35$, respectively). Moreover, the number of place cells (cells significantly modulated by location) was higher in the control group than in the KD group only in the start and goal areas (Fig. 6L; Fisher's exact test, $P = 0.027$, $P < 0.001$, $= 1$, $= 0.45$, and $= 0.49$, respectively, from left to right). These results suggest that TRPC4 KD selectively impairs the spatial representation when animals stay in a place, and place cells need to fire persistently. These suggest that TRPC4 KD specifically affects the maintenance of spatial representation when animal remained at the same place.

Additional analyses indicated that the compromised spatial representation observed in the start and goal areas in the TRPC4 KD animals is not associated with a lower running speed or weaker theta oscillations (fig. S4). These spatial analyses are in line with the time-domain analysis (Fig. 4), which revealed a specific effect of TRPC4 KD on cellular activity during, but not before or after, the delay.

Gradual decrease of left and right goal representation

We further analyzed cellular activity and spatial representation in the goal areas (Fig. 7) since the encoding of left versus right goals in the hippocampus may be crucial for task performance (*43*). First, we tested whether persistent activity differed in the goal areas using both sample and choice phases. We limited our analysis to trials in which animals spent at least 10 s continuously within the goal area (see Materials and Methods for details). Figure 7A shows the *z*-scored firing rate of all cells where the time 0 to 10 s corresponds to the 10-s period when animals continuously stayed in the left goal area (indicated by the orange line on the top). The activity of the top 10% cells was significantly lower in the TRPC4 KD group, both in the left and right goals (Fig. 7, B and C; WRS test, $P < 0.001$ and $P < 0.001$ for the left and right goals, respectively).

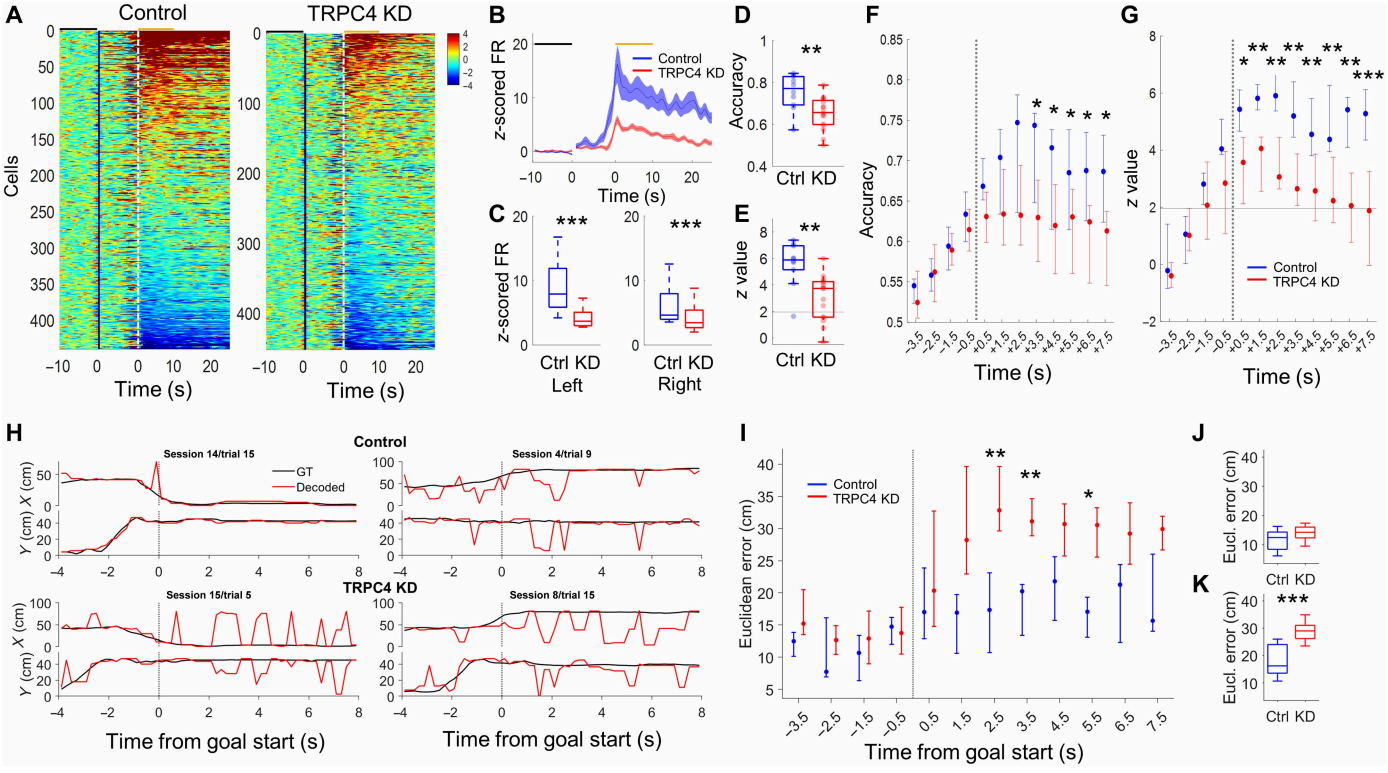


Fig. 7. Gradual decrease of the spatial representation in the goal areas in TRPC4 KD mice. (**A**) *z*-scored firing rates of cells sorted by their activity during the 10 s goal period when animals continuously stayed in the left goal area. The black vertical gap separates the first 10 s, which is referenced to the end of the ITI period, and the rest, which is referenced to the moment of the goal entry. The black and orange horizontal lines on the top indicate the baseline and the 10-s goal period, respectively. (**B**) Activity of the top 10% cells in (A). (**C**) Comparisons of activity of the top 10% of cells during the 10-s goal period (0 to 10 s) at the left and right goals. (**D** and **E**) Accuracy (D) and *z* values (E) of the SVM prediction for left versus right goals based on the activity of all cells in individual sessions during the 10-s goal period. The horizontal line in (E) indicates the 5% significance level. (**F** and **G**) Accuracy (F) and *z* values (G) of the SVM prediction for left versus right goals at different time periods before and during the 10-s goal period. The vertical dotted lines indicate goal entry, and the horizontal line in (G) indicates the 5% significance level. (**H**) Example real [ground-truth (GT)] and decoded *X* and *Y* positions of mice from 4 s before to 8 s after goal entry. The dashed lines indicate the time of goal entry. (**I**) Decoding error measured as the distance between the true and estimated positions at different time periods before and during the goal period. (**J** and **K**) Comparison of the error distance between the control and KD groups before (−4 to 0 s) and after (0 to 8 s) goal entry.

These results indicated that TRPC4 KD reduced the continuous activity of cells in the goal area as in the start area.

Next, we investigated whether this affected the representations of the left and right goals at the population level using an SVM (Fig. 7, D and E). This analysis was conducted using the activity of all cells from the 10-s goal period in each recording session with a minimum of 15 cells (n = 15 and 14 sessions in the control and KD groups, respectively). The left versus right goal prediction accuracy and z values of the SVM analysis were significantly lower in the TRPC4 KD group [Fig. 7, D and E; WRS test, $P = 0.0066$ and 0.0017 in (D) and (E), respectively]. While 90.0% of sessions had significantly higher prediction accuracy than chance level in control, only 68.8% were significantly higher than chance level in the KD group (Fig. 7E), suggesting that representations of left versus right goals may have been compromised in the TRPC4 KD group.

We further investigated whether a gradual decline in left and right goal representation may be detected over time within the 10-s goal period owing to the lack of persistent activity in the TRPC4 KD group (Fig. 7, F and G). We performed a similar SVM analysis at different time points starting from the pregoal period (−3.5 s) using a sliding (1 s) 5-s window (time indicated in Fig. 7, F and G, is the center of the window). The prediction accuracy increased over time as the animal approached the goal area (−3.5 to +1.5 s, note that +1.5 still includes 3 s of pregoal time). The prediction accuracy and z values between the control and KD groups differed significantly over time; the difference emerged starting at +3.5 s for prediction accuracy (Fig. 7F) and at the moment of entry into the goal area for the z values (Fig. 7G). These findings indicate a faster decline in the goal representation in the KD group.

To test more directly the effect of TRPC4 KD on hippocampal spatial representations at the goal areas, we used Bayesian decoding of animal's position based on the population activity (see Materials and Methods and Fig. 7, H to K). In each trial, the actual position of the mouse (black trace) was compared with the decoded position (red trace) from 4 s before goal entry, when mice were in the stem and top of the T parts of the T-maze, until 8 s after the goal entry (Fig. 7H). While the position estimation was in general good in both control and TRPC4 KD group mice before the entry to the goal area, estimation errors increased in the TRPC4 KD group after the entry to the goal area (Fig. 7I). The estimation error between control and KD mice was not different before the entry to the goal area (−4 to 0 s; Fig. 7J; WRS test, $P = 0.19$) but was significantly larger in the KD group after the entry (0 to 8 s; Fig. 7K; WRS test, $P < 0.001$). This is in line with the data in the previous section where the spatial information was not different in the stem and the top of the T parts but was smaller in TRPC4 KD group in the goal areas. Together, these suggest the specific role of TRPC4 channels on the maintenance of spatial representation.

We further investigated whether these differences between the control and TRPC4 KD mice at the goal locations existed in both the sample and choice phases (figs. S5 and S6). While statistical significance decreased in some comparisons due to the reduced number of trials in each analysis, similar results were observed in both the sample and choice phases. This agrees with the idea that persistent firing supports immediate spatial representation rather than working memory–related information storage.

Behavioral relevance

Next, we asked whether neural activity at the goal differed between correct and error trials using the same 10-s goal period from recording sessions with at least one error trial. Since goal-related activity during the choice phase cannot, in theory, affect the trial outcome, this analysis focused on goal activity during the sample phase. Because the much smaller number of error trials compared to correct trials, the activity between correct and error trials was compared using a bootstrap resampling procedure across all available recording sessions (see Materials and Methods for details). For each of the 1000 bootstrap iterations, a sample was generated by randomly drawing the same number of correct trials as there were error trials from the pool of correct trials. The activity of each cell was calculated as the average z-scored firing rate within the 10-s goal period of the selected trials. Differences between the correct and error trials were then assessed on the basis of the comparison between the single metric value obtained from the error trial set and the 1000 values constituting the bootstrap distribution of correct trials.

We first compared the distribution of the z-scored firing rates of all cells in the error trials (magenta) against those from all 1000 sets of subsampled correct trials (represented as a gray density plot) in the control mice (Fig. 8A). The error trials had a narrower distribution of z-scored firing rates than most of those from the randomly chosen correct trial sets, which is characterized by a steeper transition, indicating more cells near zero and fewer cells with highly positive or negative z-scored firing rates. To quantify this, we measured the width of the distribution using the interdecile (10th to 90th percentile) range and the interquartile range. The interdecile and interquartile ranges were both significantly narrower in the error trials compared to the correct trials for both left and right sample goals (Fig. 8B; left and right goal interdecile range, $P = 0.014$ and 0.004, respectively; left goal interquartile range: correct: 1.35 ± 0.0035, error: 0.11, $P = 0.034$; right goal interquartile range: correct: 1.49 ± 0.0027, error: 1.19, $P = 0.001$), similarly to the narrower distribution observed in the KD group compared to the control group in fig. S2A.

We next compared the fraction of cells with a z-scored firing rate larger than 1.5, which was significantly smaller in error trials than in correct trials for both left and right trials, indicating that there were fewer highly active cells in error trials (Fig. 8C; $P = 0.029$ and 0.014 for the left and right goals). The average activity of the top 10% of cells, a metric used in our other figures (e.g., Fig. 7B), was not significantly different in this analysis due to a subset of cells with exceptionally large z-score values (~20 to 30) that disproportionately contributed to the average value. We suspected that this was driven by the substantially lower number of trials included in each bootstrap iteration and the smaller number of cells available in this analysis, given that we could only include sessions with at least one error trial for a specific goal position (left and right). When these outliers were removed based on Tukey's outlier criterion (see Materials and Methods), the average activity of the top 10% of cells was significantly lower in error trials compared to correct trials for both left and right goals (Fig. 8D; $P < 0.001$ and 0.007 for the left and right goals, respectively).

These differences between correct and error trials were less pronounced in the TRPC4 KD mice (Fig. 8, E to H). The interdecile range for error trials was significantly different only for the right goal (Fig. 8F; $P = 0.62$ and 0.003 for the left and right goals, respectively), and the interquartile ranges were not significantly different in either direction (left goal interquartile range: correct: 1.11 ± 0.0026, error: 1.27 $P = 0.97$; right goal interquartile range: correct: 1.26 ± 0.0026, error: 1.14, $P = 0.069$). The percentage of cells with a z-scored firing rate larger than 1.5 SD was not significantly smaller in error trials for either the left or right goal (Fig. 8G; $P = 0.49$ and 0.08 for the left and

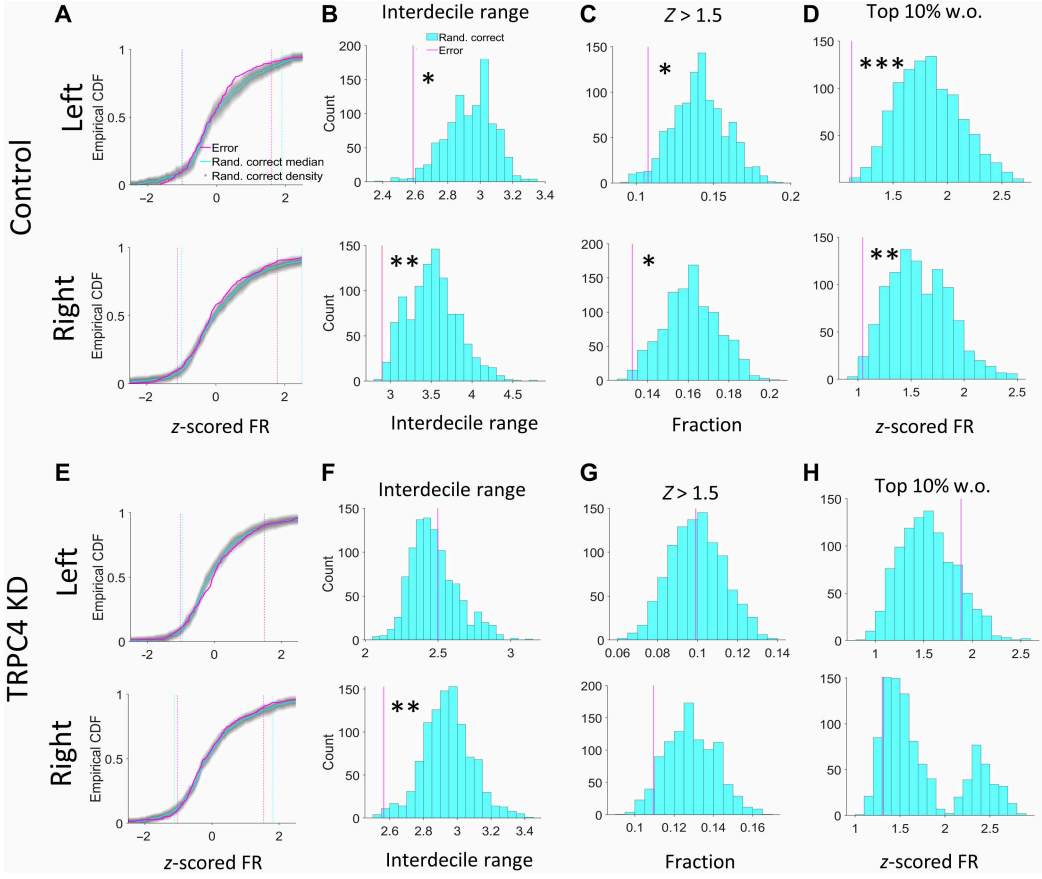


Fig. 8. Difference in cellular activity between correct and error trials at the sample goal. (**A**) Cumulative distribution function (CDF) of the mean *z*-scored firing rate (ZF_{ind}, see Materials and Methods) over the 10-s goal period for all recorded cells. Upper and bottom panels correspond to the left and right sample goals, respectively. Magenta: CDF of error trials; gray-scale density plot: CDF of 1000 sets of randomly subsampled correct trials shown as density; cyan: median CDF of all subsampled correct trials. Dotted vertical lines indicate the 10th and 90th percentile crossings for the error trial set (magenta) and the median of the correct trial sets (cyan). (**B** to **D**) Comparison of three metric values between the correct and error trials. In each panel, the magenta line indicates the metric value from error trials, and the cyan distribution represents the bootstrapping distribution of the metric values from 1000 sets of randomly subsampled correct trials. (B) Interdecile (10th to 90th percentile) range. (C) Fraction of cells with a *z*-scored firing rate larger than 1.5. (D) Average *z*-scored firing rate of the top 10% most active cells without outliers (w.o.). (**E** to **H**) Same as (A) to (D) but for the TRPC4 KD group.

right goals, respectively). Similarly, the average activity of the top 10% cells (without outlier cells) was not significantly different (Fig. 8H; $P = 0.86$ and 0.11 for the left and right goals, respectively). Together, these results indicate that the activity of cells at sample goal locations is more narrowly distributed, having a fewer number of strongly activated or suppressed cells, especially in the control group. This is consistent with the idea that hippocampal goal activity during the sample phase contributes to task performance by supporting the encoding of left versus right trial types (*43*, *45*). The somewhat less clear difference between correct and error activity in the TRPC4 KD mice could reflect a generally compromised goal representation and is in line with their near chance–level task performance.

These analyses indicated that there are differences in cellular activity between correct and error sample trials during the initial 10 s spent at goal locations. On the other hand, since our analyses in Fig. 7 suggested that the left versus right goal representation deteriorates over time and more quickly so in the TRPC4 KD mice, the amount of time spent at the sample goal might have affected task performance. To test this, we compared the time animals spent at the goals between correct and error trials (fig. S7). This goal duration was generally longer in the error trials, but it was not significantly different in the control mice (fig. S7A), whereas it was slightly but significantly longer in the error trials for the TRPC4 KD group (fig. S7B). In contrast, during the choice phase, animals spent a longer time in the correct trials, probably due to the fact that a food reward was given only in these instances (fig. S7, C and D). The longer time spent at the sample goal during error trials, especially in the TRPC4 KD group, is in line with the idea that an increasingly compromised goal representation during a long-duration goal period results in erroneous left versus right trial-type encoding and leads to a wrong arm choice in the upcoming choice phase.

Selective behavioral relevance at goals

Last, we asked whether these reductions in metric values during error trials were limited to the sample goal phase or could also be observed across other phases of the task. We tested this across five distinct task segments using the bootstrap resampling method (fig. S8): (i) the ITI preceding the trial (ITIp), (ii) the sample goal (GLs), (iii) the

delay period, (iv) the choice goal (GLc), and (v) the ITI following the trial (ITIr).

First, the interdecile range of the *z*-scored firing rates from correct and error trials was compared in control mice (fig. S8A). In this plot, values above zero indicate that the correct trial metric was larger than that of error trials because the *y* axis is expressed as the difference relative to the error trial value. The red horizontal line at $y = 0$, therefore, indicates the interdecile range from error trials set, while the violin plot represents the bootstrap distribution of the interdecile range for correct trials sets. We observed that the interdecile range during the sample goal phase (GLs) was significantly smaller in error trials than in correct trials for both left and right goals. During the choice goal phase (GLc), only the right goal interdecile range was significantly smaller in error trials than in correct trials. In contrast, the interdecile range of error trials was not significantly smaller than that of correct trials during the ITI preceding the trial (ITIp), the delay period, or the ITI following the trial (ITIr). Together, these findings indicate a goal-specific reduction of activity during error trials.

In agreement with this pattern, the proportion of cells with a *z*-scored firing rate greater than 1.5 was significantly smaller in error trials during both the left and right sample goal phases and the right choice goal phase, while there were no significant reductions during the ITI and delay periods (fig. S8B). The average *z*-scored firing rates of the top 10% of cells (with outliers removed) mirrored this pattern in control mice (fig. S8C). In contrast, within the TRPC4 KD group, a significant reduction was observed exclusively for the interdecile range during the right sample goal and left and right choice goal phases (fig. S8D). Together, these results highlight the importance of goal-phase cellular activity to task performance over the activity observed during the ITI and delay periods.

In summary, our data suggested that the intrinsic mechanism of persistent firing supports a stable spatial representation of goal locations, which is necessary for correct encoding of left versus right turns.

DISCUSSION

Despite empirical evidence (*19*, *21*, *24*, *46*) and theoretical supports (*26*–*28*), it remained unclear whether individual cells support persistent activity in vivo. We identified the TRPC4 channel as a molecular mechanism of intrinsic persistent firing in CA1 pyramidal cells (*25*) and demonstrated that persistent firing was significantly reduced in vivo in a spatial working memory task by TRPC4 KD (Figs. 2 and 3). These results provide the initial direct evidence that a single-cell mechanism supports persistent firing in vivo during a cognitive task. Further analyses revealed a specific effect of TRPC4 KD on persistently firing (Fig. 4) without disrupting signal-to-noise ratio in general. The behavioral outcome align with studies indicating the role of TRPC channels (*47*, *48*) and manipulations that potentially disrupt persistent firing (*32*) in working memory.

Classically, persistent firing during the delay period has been believed to hold working memory content. Abundant evidence supports this in the prefrontal cortex and hippocampus during the working memory delay period in humans and monkeys (*5*, *8*) whereas data in rodents remains mixed (*35*, *44*, *49*). In agreement with these rodent studies, our SVM analyses suggest the absence or very weak presence of working memory content in the delay phase (Fig. 5). An alternative theory posits that the hippocampus contributes to this type of working memory task by providing spatial information during the sample phase to help encoding, rather than maintaining working memory content (*43*, *50*, *51*). We found that neurons with strong persistent firing had larger spatial information, and TRPC4 KD reduced spatial information specifically in places where persistent firing was observed (start and goal areas), suggesting that persistent firing mainly codes for spatial information (Figs. 6 and 7).

Hippocampal place cells are believed to be supported by path integration, which requires the maintenance and continuous updating of spatial representation (*40*). Computational studies have suggested that similar attractor networks, such as continuous attractor networks, support working memory and path integration (*37*, *38*). The continuous attractor model maintains spatial representation by persistent firing of a subset of neurons, "bump of activity," through recurrent synaptic networks (*38*). However, the neural networks of CA1, where place cells were most intensively studied, and MEC layer II, where grid cells were found, lack recurrent excitatory networks (*52*, *53*). In addition, these network models are sensitive to distractors, whereas experimental evidence suggests their robustness to distractors (*54*, *55*).

Including the intrinsic cellular mechanisms of persistent firing in attractor networks to form a "hybrid model" has been shown to ameliorate these problems increasing stability against noise, reducing drift, and reducing sensitivity to parameters (*28*, *29*, *56*). Upon empirically disrupting the intrinsic mechanism of persistent firing in vivo, we observed that the spatial representation was compromised specifically at the start and goal areas. The preservation of spatial representation in other areas may indicate that attractor dynamics were still present, which is in agreement with the hybrid model. The gradual degradation of the goal representation in the TRPC4 KD mice (Fig. 7) suggests a drift of the attractor state due to the loss of the persistent firing mechanism in individual cells, as predicted by the loss of intrinsic properties in the hybrid model (*28*).

An intact spatial representation outside the start and goal areas can be supported by external cue-based navigation (*57*) that may not require information retention by persistent firing. Distal cues on the surrounding curtains and walls were visible to animals when they were in long corridors such as the stem and return arms, which was not the case in the start and goal areas. Alternatively, this could be attributed to the time required for persistent firing initiation, owing to the $Ca2^{+}$-dependent biochemical processes involved in activating TRPC channels (*20*). When the mice ran through the T-maze arms at a relatively high speed, the resulting short period of activation of each place cell may not have been long enough to fully activate the TRPC channels. Further studies are needed to clarify the exact mechanisms TRPC4 supports spatial representation specifically when mice remained at fixed locations.

Hippocampal spatial coding during immobility remains less understood than coding during active locomotion. While early work indicated that place cell firing ceases when animals are restrained (*58*), Kay and colleagues (*59*) more recently found spatially tuned hippocampal cells that continue to fire during periods of immobility in freely behaving rats. Although their study primarily focused on CA2 cells, they reported that similar immobile spatial coding exists within the CA1 and CA3 subfields, with cells sustaining their spiking while the animal is stationed at one of the wells in a W-maze. It is therefore possible that these cells overlap or share common mechanisms with the persistent firing cells we report here.

Nevertheless, several notable differences exist between these prior findings and our current results. First, the locomotor activity of

the mice in our study appeared to be more elevated; animals actively moved within the start or goal areas with an average speed of 3 to 5 cm/s (fig. S4, A to D), whereas Kay and colleagues (*59*) reported speeds below 4 cm/s, often close to complete stop. Second, while theta oscillations remained visible in the start and goal locations in our study (fig. S4, E to J), Kay and colleagues (*59*) observed these spatial cells primarily during non-theta periods. Yuan and colleagues (*13*) have specifically demonstrated that the persistent firing of CA1 cells during the delay period of a working memory task is independent of both running speed and theta power, suggesting that persistent activity itself can be decoupled from locomotion and theta rhythms. However, a systematic evaluation of the role of theta oscillations in hippocampal spatial representation during immobility is currently lacking. Last, Kay and colleagues (*59*) showed that the firing of these immobile spatial cells correlates with specific local field potential (LFP) features that reflect coordinated network activity across CA1, CA2, CA3, and the dentate gyrus, suggesting that spatial representation during immobility may involve inter-regional computation.

Together, these findings suggest that future investigations into spatial representations within immobile or confined spaces should systematically evaluate the interplay between running speed, LFP states, and network-wide computation, and how these factors relate to TRPC4-based intrinsic cellular mechanisms. Furthermore, while the current study focused on the role of persistent firing in a spatial working memory task, we cannot exclude the possibility that other hippocampal electrophysiological phenomena—such as sharp-wave ripples (*60*), theta-phase precession (*61*), and theta-gamma coupling (*62*)—could have also been compromised by the TRPC4 KD and consequently affected task performance. Characterizing these electrophysiological phenomena will be essential to fully comprehend the spectrum of downstream effects exerted by TRPC4 KD.

We have shown that cellular activity at the goal during the sample phase was different between correct and error trials, especially in the control mice (Fig. 8). The cellular activity of control mice in error trials resembled that of the TRPC4 KD mice in the sense that the cells showed a narrower distribution of their *z*-scored firing rates, and fewer cells had strong activation in comparison to the correct trials. This is in line with the previously proposed idea that the hippocampus supports spatial working memory tasks by providing spatial information during the sample phase to help with the encoding of left versus right trial types, thereby helping to correctly choose the arm to enter in the upcoming choice run (*43*, *50*, *51*).

Further analysis comparing correct versus error trials revealed that this difference in activity was not seen during the ITI or delay periods, further stressing the importance of goal-related activity (fig. S8). However, the fact that the difference was observed in both the sample and choice goal phases (fig. S8, A to D) is counterintuitive because the choice goal phase occurs after the animal chooses the left or right arm; thus, this activity cannot influence task performance. We discuss that this result indicates at least two potential scenarios. First, it could be that the animal was not attending to the task during error trials, resulting in low acetylcholine (ACh) levels throughout the entire trial, which subsequently affected both sample and choice goal activity. While this leaves it unclear why delay period activity, which occurs between the sample and choice goals, was not affected, intrinsic persistent activity can be supported by other neuromodulators or metabotropic glutamate receptor activation (*63*). Therefore, it could be that these mechanisms were somehow sufficient to maintain delay period activity. The second possibility is that the difference in activity at the choice goal could simply be triggered by the food reward. While animals received a food reward during both correct and error trials at the sample goal, they only received a reward during correct trials in the choice phase. It has been reported that acetylcholine levels increase at goals associated with reward in a T-maze task similar to ours (*64*). In this scenario, our data suggest that behavioral errors occur specifically when sample-phase goal activity is compromised—potentially due to a phasic decrease in ACh levels (*65*). To distinguish between these possibilities, simultaneous measurements of acetylcholine signaling and cellular activity will be essential in future studies.

In addition, it should be emphasized that the difference between correct and error trials demonstrated here represents a correlational, rather than a causal, link between goal-related activity and task performance. Therefore, it remains possible that behavioral errors are driven by other cellular mechanisms, such as impaired synaptic plasticity due to reduced acetylcholine levels occurring simultaneously with attenuated persistent activity. To establish a causal link, future studies would benefit from manipulating TRPC4 channel conductance or persistent firing with greater temporal resolution on a trial-by-trial basis.

The prevailing view that neurons fire only when they receive sufficient input dictates current understanding of neural computation in the brain. Our findings challenge this view, revealing them as active contributors to information retention in vivo. This intrinsic persistent firing depends on the cholinergic system, which degrades in aging and Alzheimer's disease (*66*, *67*) causing cognitive impairments (*68*, *69*). Our findings thus potentially reshape our general understanding of brain computation and highlights novel therapeutic targets for cognitive disorders.

MATERIALS AND METHODS

Animals

Twelve-week-old C57BL6/J male mice were obtained from a local animal facility. The mice were group-housed until the time of surgery and individually housed thereafter to avoid injury to sutures and/or implants. A 12-hour light/12-hour dark cycle was used, and the mice underwent experiments during the light cycle. Mice housing room conditions were maintained at 21° to 24°C and 40 to 50% humidity. All experimental procedures were performed in accordance with animal research permission (TVA) obtained from the animal committee of Sachsen-Anhalt (Landesverwaltungsamt Referat Verbraucherschutz, Veterinärangelegenheiten, Az. 42502-2-1388 DZNE, 203.m-42502-2-1665 DZNE).

TRPC4 channel KD

We developed a TRPC4 shRNA-expressing virus (TRPC4_AAV_U6_shRNA2_GFP) to knock down TRPC4 channels and a scramble virus (AAV_U6_scramble_GFP) for the control experiments. Oligos for TRPC4 were designed based on Puram and colleagues (*70*) and were ordered from Sigma-Aldrich. The following oligonucleotides were used to clone small interfering RNA (siRNA) against mTRPC4 into AAV_U6_GFP:

mTRPC4_siRNA2: siRNA_TRPC4_Mouse/Human_2: Sense and antisense

5′-GATCCGGTCAGACTTGAACAGGCAATTCAAGAGATTGCCTGTTCAAGTCTGACCTTTTTTG-3′

3′-GCCAGTCTGAACTTGTCCGTTAAGTTCTCTAACGGACAAGTTCAGACTGGAAAAAACTTAA-5′

Adeno-associated virus (AAV2) and U6 were used as the vectors and promoters, respectively. After purification, the titers were checked by quantitative polymerase chain reaction (qPCR) (using TaqMan probes) and different dilutions. The titer for TRPC4_AAV_U6_shRNA2_GFP was 4.03×10^{12} and for AAV_U6_scramble_GFP was 3.56×10^{12}. Last, primary hippocampal cell cultures were infected with either no virus, scrambled virus, or TRPC4 KD virus, and a significant reduction in TRPC4 mRNA expression by the TRPC4 KD virus was confirmed by reverse transcription qPCR (Fig. 1A).

Surgery

C57BL/6JCrl male mice were weighed and anesthetized using a ketamine and xylazine cocktail [ketamine (20 mg/ml) + xylazine (2.5 mg/ml), 0.1 ml/20 g]. The head was fixed in the stereotactic device ~10 min after anesthetic injection. Head hair was completely removed, and the head was scrubbed using betadine (povidone-iodine) and ethanol 70%. A small incision was made using a scalpel, and the tissues were gently retracted. The skull position was checked horizontally. The Bregma point was used as reference, and the injection sites were marked according to coordinates from Paxinos atlas (AP: −2.1, ML ± 1.7, DV: 1.1 and AP: −2.7, ML ± 2.5, DV: 1.5). The marked points were drilled with a 0.7-mm drill tip. TRPC4_AAV_U6_shRNA2_GFP or AAV_U6_scramble_GFP viral particles were injected using a Hamilton neuro syringe (1701, 33-gauge needle) and stereotaxic syringe pump (CHEMYX, NANOJET) to control injection speed (100 nl/min) and volume (1 μl per site). The needle remained at the injection site for 5 min before retraction. Next, the skin was closed using veterinary surgery glue, and carprofen (5 mg/kg) was subcutaneously injected. Metamizole (200 mg/kg) was added to a 100-ml water bottle. The mice were allowed to recover for a few hours in the surgery room and then transferred to the animal room. They were checked daily (for 3 days) for recovery and pain management.

For in vivo electrophysiological experiments, a microdrive with eight tetrodes was implanted on the right hemisphere and lateral to the virus injection site (AP: −2.1, ML ± 1.8, DV: 0.6). Four anchor screws and one ground screw are affixed to the skull. The implant was fixed using acrylic dental cement.

In vitro neural recordings

The mice were deeply anesthetized with isoflurane, and the brains were quickly extracted after decapitation. Brains were placed in ice-cold cutting solution containing 110 mM Choline Cl, 7 mM $MgCl_2$ ($6H_2O$), 0.5 mM $CaCl_2$, 2.5 mM KCl, 25 mM glucose, 1.2 mM NaH_2PO_4, 25 mM NaHCO3, 3 mM pyruvic acid, 11.5 mM ascorbic acid, and 100 mM D-mannitol. A Leica VT-1000 vibratome was used to obtain 350 μM coronal slices. Brain slices were transferred to a holding chamber containing normal ACSF (nACSF) containing 126 mM NaCl, 1.2 mM NaH_2PO_4, 26 mM $NaHCO_3$, 1.5 mM MgCl2, 1.6 mM $CaCl_2$, 3 mM KCl, and 10 mM glucose. Slices were submerged for 30 min at 37°C and then transferred to another holding chamber at room temperature for at least 30 min before recording.

Brain slices were transferred to the recording chamber and continuously superfused with nACSF (34.5° ± 1.5°C). The cells were visualized using an upright microscope (Olympus BX51WI) with a 40× water immersion objective and a Thorlabs CS895MU monochrome camera. Green fluorescent protein–positive (GFP^+) cells were located by exciting GFP with a 470-nm wavelength LED (CoolLED PE 4000) through a filter cube with excitation filter of 469 ± 17.5 nm, dichroic of 452 to 490 nm/505 to 800 nm, and emission filter of 525 ± 19.5 nm. Whole-cell configuration was achieved using 3- to 5-MΩ patch pipettes filled with intracellular solution containing 120 mM K-gluconate, 10 mM Hepes, 0.2 mM EGTA, 20 mM KCl, 2 mM $MgCl_2$, 7 mM PhCreat di(tris), 4 mM Na_2ATP, and 0.3 mM tris-guanosine 5′-triphosphate (pH adjusted to 7.3 with KOH). For labeling purposes, 0.1% biocytin was added to the intracellular solution. Access resistance was monitored and compensated for several times during recording. The liquid junction potential was not corrected. Electrophysiological signals were amplified using a Multiclamp 700A amplifier and digitized using an Axon Digidata 1550 B. Current clamp recordings were routinely filtered at 10 kHz and sampled at 20 kHz using pClamp 11 software. After recording, the slices were stored at 4°C in a phosphate-buffered saline (PBS) solution with 4% paraformaldehyde (PFA).

Behavioral task

The spatial working memory task in the T-maze was started 4 weeks after virus injection. Before this test, the mice were handled for 3 days to habituate to the experimenter. Mice were food-deprived at the start of handling to motivate them for the reward, and reward pellets were introduced to them before starting the main experiment. Animal weight was maintained between 85 and 90% of body weight before food deprivation. Second, habituation to the T-maze (OHARA Ltd., Japan) was performed for 3 days.

Each animal was tested for 10 days, with each day constituting 10 trials (10 sample + 10 choice phases). Each trial started with a sample trial (forced trial), in which the T-maze software assigned the left or right door (at the T-junction) to open randomly. First, the start door was opened, and the mouse moved from the start area to the stem, open arm (top of the T-maze), and goal area where it received the reward. Next, the animal returned to the start area using the return arm and waited for 30 s (delay period). After the delay, the choice trial began; this time, both the left and right arms were open, and the mouse chose the arm opposite the sample trial. If the trial was successful, then the animal received a pellet at the goal location. After collecting the reward, the animal moved back to the start area, where a new trial began after 45 s (ITI). After each experiment, the maze floor was cleaned with 10% ethanol, and the walls were cleaned with water. Behavioral data were analyzed using MATLAB (MathWorks) and SPSS (IBM).

In vivo neural recordings

Tetrodes were made using 12.5-μm Tungsten wire (California Fine Wire Co.) and grouped in a single bundle with eight tetrodes (32 channels) inside a microdrive (AXONA). The tetrodes were gold-plated using nanoZ (White Matter LLC, USA) in gold solution to reduce the impedance to 150 kΩ.

Screening was conducted 7 to 10 days after surgery and after handling the animals to place the tetrodes in the pyramidal layer of CA1. Screening was performed in an open-field arena (30 cm by 30 cm, shielded and grounded). The presence of place cells, autocorrelation, firing frequency, and waveform characteristics were the criteria used to identify the pyramidal layer. Once the tetrodes were in a position or very close to CA1, the behavioral experiment in the T-maze began.

Single-unit activity and LFPs were recorded using an in vivo electrophysiology setup (Axona Ltd.). The data were recorded in the raw mode at a sampling rate of 48 kHz. To obtain single-unit spike data, raw data were referenced and band-passed (400 to 8000 Hz) using custom scripts written in MATLAB (MathWorks), and spikes were

detected using TINT (Axona Ltd.). The detected spikes were clustered using KlustaKwik (*71*) for automatic clustering, and manual curation of the clusters was performed using the Klusters software (Lynn Hazan). LFP data with a 4800-Hz sampling rate were created using TINT (Axona Ltd.). The position of the mouse was tracked at 50 Hz using a video camera that recorded the position of a light-emitting diode attached to the mouse head.

Histology

Mice were anesthetized with a ketamine and xylazine cocktail and transcardially perfused with cold PBS (4°C, 15 ml) and then cold 4% PFA (pH ~ 7.4, 50 ml). Brains were removed and post-fixed in 4% PFA at 4°C for 24 hours. After applying the cryoprotective protocol (1 day in 10% sucrose and 3 days in 30% sucrose), samples were embedded in cubic molds filled with Optimal Cutting Temperature compound and then snap frozen. Next, the samples were transferred to the −80°C freezer for storage. The fixed samples were sectioned using a cryostat. The slices were then covered and mounted using a mounting medium. Images were obtained with a confocal microscope (Zeiss, AxioImager M2) and fluorescence microscope (Keyence, BZ-X710) using 2.5×, 5×, and 40× objectives to control for virus expression and tetrode traces (fig. S1).

In vitro data analysis

The resting membrane potential was measured by averaging the membrane potential for 1 min after seal opening without current injection. Input resistance was calculated using Ohm's law, measuring the voltage deflection in response to a negative current pulse of −50 pA at −65 mV. Intrinsic excitability was evaluated by counting the number of action potentials during the positive step-wise current injections (1 s), from −300 to 300 pA in 50-pA jumps (IV protocol). The adaptation index was calculated by dividing the instantaneous frequency of the last pair of action potentials by the instantaneous frequency of the second pair of action potentials in the first sweep, with at least 10 action potentials in the IV protocol. In vitro persistent firing was induced by a 2-s 100-pA current injection at a voltage level of 5 to 3 mV below the action potential threshold. The strength of persistent firing was evaluated by calculating the average firing frequency and depolarization in the first 10 s poststimulus. The cells were classified as having long (>30 s), short (<30 s), or no persistent firing based on the duration of persistent firing observed (measured from the offset of the stimulus).

In vivo data analysis

The data were analyzed using custom-written MATLAB scripts and the CMBHome toolbox developed at the Center for Memory and Brain, Boston University.

Temporal binning and z-score firing rate

The time-binned firing rate of each cell was prepared using a 0.5-s bin and smoothed with a 2.5-s Gaussian window to analyze in vivo persistent firing. The *z*-scored firing rate was calculated from the time-binned firing rate data using the following equation

$$Z = \left[f - mean(F)\right] / std(F) \quad (1)$$

where *f* and F are the binned firing rates from the period of interest and baseline period, respectively.

Cell-type classification based on activity change

Neurons were classified into activated (Act), suppressed (Sup), and nonmodulated (NM) cells, according to the delay period activity (Fig. 2E) (*72*). The binned firing rate at baseline (15 to 5 s before the delay) was compared to the activity during the delay (0 to 25 s) using the WRS test. Cells were considered to be modulated if the test result was significant ($P < 0.01$). The *z* value obtained during the test (WRS *z* value) was used to classify the modulated cells into the Act (WRS *z* value > 2.58) and Sup (WRS *z* value < −2.58) groups. The remaining cells were classified as NM. The WRS *z* values were used to plot a histogram, as shown in Fig. 2E.

Temporal field

The peak *z*-scored firing rate during the delay period was determined to define the temporal field for each cell. The temporal field duration was defined as the time when the *z*-scored firing rate was continuously above 10% of the peak value (Fig. 2I). In Fig. 3, the temporal field duration is defined in the same way using the raw firing rate instead of the *z*-scored firing rate.

SVM analysis

A population vector was built for each trial of each session using neuronal activity during the delay period (0 to 25 s) or from the goal area (0 to 10 s). Single-unit spike activity was temporarily binned (0.5-s bin) for left versus right and ITI versus delay comparisons. A temporal bin size of 0.02 s was used for the left versus right goal comparison with a 5-s sliding window (Fig. 7, F and G). Each trial was then labeled according to the type of test: ITI versus delay or left versus right (retrospective or prospective). Only sessions with at least 15 units were included in the analysis.

Binary SVM comparisons were performed for each session with the fitcsvm function (MATLAB) using a linear kernel and twofold cross-validation of the input data to evaluate model performance. The model was run 30 times, and the obtained balanced accuracies were averaged. To evaluate the significance of the prediction, the class labels were scrambled, and the SVM model was run for the nonscrambled data a minimum of 30 times (sessions where label permutation did not generate at least 30 different combinations were not included in the analysis). Moreover, a random accuracy distribution was built and then used to determine the *z*-scored balance accuracy. Sessions with *z*-score > 1.96 were considered to have above-chance accuracy.

Spatial information and place cells

Spatial information (SI) is defined as the extent to which the firing of a cell can be used to predict the position of the animal. The SI was calculated using the formula of Skaggs *et al.* (*73*)

$$SI = \int_{\infty} \lambda(x) \log_2 \frac{\lambda(x)}{\lambda} p(x) dx \quad (2)$$

where SI is the information rate in bits/s, x is the spatial location of the animal, $\lambda(x)$ is the mean frequency at location x, $p(x)$ is the probability of finding the animal at a given location in the maze, and λ is the overall firing rate of the cell.

Spatially modulated cells were selected by building a randomized distribution of spatial information values obtained by circularly shifting the spike timing and position vectors for at least 20 s 100 times. Cells with spatial information above the top 95% of the random distribution were considered spatially modulated cells (place cells).

The spatial rate maps represent the average firing rate of a cell at a given location and were obtained by dividing the number of spikes at a location by the total time that the animal spent at that location (occupancy). Rate maps were calculated using 1 cm–by–1 cm bins, and the data were smoothed using a two-dimensional (2D) convolution with a Gaussian kernel with a 2.5-cm standard deviation. Only bins with speed greater than 2.5 cm/s were considered in the calculation.

Place field centers were detected as follows. First, pixels of a rate map with a high firing rate (>4 SD) were extracted. Extracted rate map was processed with the regionprops function (MATLAB) to detect and characterize the individual fields, and the area and centroid parameters were obtained. To avoid detecting noise, fields smaller than 12 or larger than 650 cm^2 were discarded, and firing field with the highest coefficient of variation was considered the main firing field of a given neuron. The coefficient of variation was calculated as follows

$$\mathrm{CV} = \frac{\text{Mean field firing rate}}{\text{SD field firing rate}} \quad (3)$$

Theta power

Theta power at the start and goal locations was calculated for each recording session as follows. First, LFP data were band-pass filtered (6 to 10 Hz) to isolate theta oscillations. The instantaneous theta power was then extracted by taking the squared magnitude of the analytic signal derived via the Hilbert transform. Last, power segments corresponding to the times when the animal was at the start (or goal) locations were concatenated and averaged.

Putative cell-type classification

Putative pyramidal neurons and interneurons were identified on the basis of the average firing rate and spike duration. Cells with an average firing rate <8 Hz and a peak-to-peak spike duration >0.255 ms were classified as putative pyramidal cells, whereas those with an average firing rate >8 Hz and a peak-to-peak spike duration <0.255 ms were classified as putative interneurons (*74*, *75*).

Trial selection for goal analysis

The duration of time animals stayed at the goal areas varied greatly from trial to trial, ranging from 1.6 to 410.0 s (median duration: 47.74 and 47.73 s for control and TRPC4 KD groups, respectively; WRS test, $P = 0.99$), because the task did not restrict the time animals spend at the goal areas. In addition, the animals returned to the top arm (top of T) in some trials. Therefore, we limited our goal analysis to trials in which the animals continuously spent at least 10 s within the goal area during the sample phase. In the control and KD groups, 89.5 and 82.3% of the trials met this criterion, respectively. When multiple such periods were found in a trial, we analyzed the first incident. The baseline period to build the *z*-scored firing rate was the last 20 s of the ITI period before goal entry. This ensured that goal activity was not included in the baseline period. In Fig. 7 (A, H, and K), the black vertical gap separates the first 10 s, which is referenced to the end of the ITI period, from the rest, which is referenced to the start of goal entry. The trials in each recording session were first divided into left and right sample goal trials to compare correct and incorrect trial activities. Subsequently, we checked whether at least one correct or incorrect trial was present for each goal location. Sessions that did not meet these criteria were excluded from the analysis.

Bayesian position decoding

For Bayesian position decoding, we included sessions with at least 30 simultaneously recorded CA1 units. In each session, position decoding was performed on trials in which the mouse stayed at the goal location for longer than 10 s because our focus was on the maintenance of spatial representation over time. In each trial, position decoding was performed using a 12-s window spanning 4 s before to 8 s after goal entry (goal window). To build spatial tuning curves for later decoding, 2D rate maps with a 1.7-cm spatial bin size were calculated for all cells using the spike data from the complement of the goal window within the session (i.e., all spike data of the session excluding the goal window from corresponding trial). Data used for decoding in each goal window consisted of spike counts from all cells binned into nonoverlapping 200-ms time bins ($\Delta t = 0.2$ s), which were smoothed across time using a Gaussian kernel (6-bin window).

Decoding assumed independent Poisson spiking across units, such that for each spatial bin (state) s with expected rate $\lambda_i(s)$ from the rate map, the log-likelihood of observing counts r_i in a time bin was computed as $\sum_i[r_i \log \lambda_i(s) - \lambda_i(s)\Delta t]$; rate-map values were floored at 10^{-6} Hz to ensure numerical stability. A uniform prior over spatial states was used, and the posterior over all spatial bins was obtained by combining log-likelihood and log-prior and normalizing each time bin.

Decoded position was taken as the maximum a posteriori (MAP) spatial bin and converted to x-y coordinates using bin centers; posterior marginals over x and y were additionally computed by summing the 2D posterior over the orthogonal dimension. Ground-truth $x(t)$ and $y(t)$ at each decoding time bin midpoint was obtained by linear interpolation of the tracked position and discretized into a spatial bin center coordinate. Decoding accuracy was quantified as the Euclidean distance between decoded and ground-truth position at each time bin.

Error-trial activity analysis

To assess differences in neural activity between correct and error trials, we used a matched-correct bootstrap procedure because the number of error trials was significantly lower than that of correct trials. Trials were classified as correct or error, and we only included sessions containing at least one error trial and a sufficient number of correct trials to match the error trial count. When analyzing the goal segments, only trials with a goal duration exceeding 10 s were included, consistent with our other goal analyses.

In each bootstrap iteration, a set of matched-correct trials was subsampled to match the number of error trials as follows. First, a subset of correct trials matching the number of error trials was randomly drawn from each recording session. Then, these subsets from all sessions were pooled to form a single set of pooled correct trials. This process was repeated 1000 times, ensuring that no two iterations contained identical combinations of trials. Because the error trial set contained all error trials from all recording sessions, this process ultimately created one fixed error trial set and 1000 different resampled correct trial sets.

Subsequently, the activity of individual cells (ZF_{ind}) was calculated for the error set and for each of the 1000 subsampled correct trial sets. This was defined as the average *z*-scored firing rate of a given cell during the defined analysis segment (e.g., the initial 10 s of the goal segment) across the trials in the corresponding trial set. The metrics used for the correct and error trial comparisons were then calculated using the ZF_{ind} from each trial set. The interdecile and interquartile ranges (e.g., Fig. 8B) were calculated from the distribution of ZF_{ind} across all cells. The fraction of cells with a z-score larger than 1.5 (e.g., Fig. 8C) was calculated by counting the number of cells with $ZF_{ind} > 1.5$ and then dividing this count by the total number of cells. The average *z*-scored firing rates of the top 10% of cells (e.g. Fig. 8D) were measured as follows. First, the mean *z*-scored firing rate during the analysis segment (e.g., the initial 10 s of the sample left goal) across all correct and error trials was calculated for each cell, independent of the bootstrap procedure. Then, outliers were excluded using Tukey's outlier criterion as stated below. From this filtered population, we identified the top 10% most active cells based on their mean *z*-scored firing rate. During the bootstrap procedure,

the average ZF_{ind} of these identified cells was calculated for the error and all bootstrapped correct trial sets. This allowed us to compare the activity of the exact same population of cells between correct and error trials.

For statistical testing, the metric from the single error trial set was compared with the metrics from the 1000 matched-correct bootstrap trial sets (the bootstrap distribution). One-sided tests were used to evaluate whether the metric in the error trial set was lower than the bootstrap distribution. Empirical *P* values were calculated with a +1 correction (*76*) to account for the finite number of bootstrap samples, thereby avoiding a *P* value of zero when no randomized value was as extreme as the observed value, as follows

$$P = \left[\#\left(\text{bootstrap distribution} \leq \text{error}\right) + 1\right] / (N + 1) \qquad (4)$$

where #(bootstrap distribution ≤ error) is the number of metric values in the N (=1000) bootstrap distribution that are smaller than or equal to the metric of the error trial set.

For the comparison of correct and error trial activity during the ITI, goal, and delay periods, the analysis segments corresponded to the initial 25, 10, and 25 s of each respective segment (fig. S8).

Statistical analysis

The data were checked for distribution and homogeneity before statistical analysis. Comparisons between groups were performed using the Wilcoxon rank-sum and Kruskal-Wallis tests. A *t* test or analysis of variance (ANOVA) followed by Tukey's post hoc test was used for normally distributed data. Multiple-comparison corrections were used where relevant. Categorical variables (group ratios) were compared using the χ^2 test or Fisher's exact test if any group had fewer than five items. Boxplots represent the median and upper and lower quartiles. Significance was expressed as follows: $^*P < 0.05$, $^{**}P < 0.01$, and $^{***}P < 0.001$. Outliers exclusion was used only for the calculation of variance in fig. S2 and the top 10% cell in Fig. 8 and fig. S8 using Tukey's outlier criterion, whereby values outside the range [Q1 − 1.5 × IQR, Q3 + 1.5 × IQR] (where IQR is the interquartile range) were removed (*77*).

Supplementary Materials

This PDF file includes:

Figs. S1 to S8

REFERENCES

1. J. H. Choi, S. Bae, J. Park, M. Yoo, C. H. Kim, L. I. Schmitt, Y. Tchoe, D. Chung, J.-W. Choi, J.-C. Rah, Short-term memory errors are strongly associated with a drift in neural activity in the posterior parietal cortex. *PLOS Biol.* **23**, e3003359 (2025).
2. N. T. M. Robinson, L. A. L. Descamps, L. E. Russell, M. O. Buchholz, B. A. Bicknell, G. K. Antonov, J. Y. N. Lau, R. Nutbrown, C. Schmidt-Hieber, M. Häusser, Targeted activation of hippocampal place cells drives memory-guided spatial behavior. *Cell* **183**, 1586–1599.e10 (2020).
3. G. Major, D. Tank, Persistent neural activity: Prevalence and mechanisms. *Curr. Opin. Neurobiol.* **14**, 675–684 (2004).
4. J. Zylberberg, B. W. Strowbridge, Mechanisms of persistent activity in cortical circuits: Possible neural substrates for working memory. *Annu. Rev. Neurosci.* **40**, 603–627 (2017).
5. J. M. Fuster, Unit activity in prefrontal cortex during delayed-response performance: Neuronal correlates of transient memory. *J. Neurophysiol.* **36**, 61–78 (1973).
6. K. Kubota, T. Iwamoto, H. Suzuki, Visuokinetic activities of primate prefrontal neurons during delayed-response performance. *J. Neurophysiol.* **37**, 1197–1212 (1974).
7. M. Colombo, C. G. Gross, Responses of inferior temporal cortex and hippocampal neurons during delayed matching to sample in monkeys (Macaca fascicularis). *Behav. Neurosci.* **108**, 443–455 (1994).
8. J. Kamiński, S. Sullivan, J. M. Chung, I. B. Ross, A. N. Mamelak, U. Rutishauser, Persistently active neurons in human medial frontal and medial temporal lobe support working memory. *Nat. Neurosci.* **20**, 590–601 (2017).
9. P. R. Solomon, E. R. Vander Schaaf, R. F. Thompson, D. J. Weisz, Hippocampus and trace conditioning of the rabbit's classically conditioned nictitating membrane response. *Behav. Neurosci.* **100**, 729–744 (1986).
10. C. E. Curtis, D. Lee, Beyond working memory: The role of persistent activity in decision making. *Trends Cogn. Sci.* **14**, 216–222 (2010).
11. E. Pastalkova, V. Itskov, A. Amarasingham, G. Buzsáki, Internally generated cell assembly sequences in the rat hippocampus. *Science* **321**, 1322–1327 (2008).
12. C. J. MacDonald, K. Q. Lepage, U. T. Eden, H. Eichenbaum, Hippocampal "time cells" bridge the gap in memory for discontiguous events. *Neuron* **71**, 737–749 (2011).
13. L. Yuan, J. F. Figueroa, A. Khan, G. Narayan, J. K. Leutgeb, S. Leutgeb, Time cell sequences during delay intervals are not dependent on brain state and do not support hippocampus-dependent working memory. *Nat. Commun.* **16**, 7470 (2025).
14. D. O. Hebb, *The Organization of Behavior; a Neuropsychological Theory* (Wiley, 1949).
15. J. F. Fulton, *Physiology of the Nervous System* (Oxford Univ. Press, 1949).
16. A. Compte, Computational and in vitro studies of persistent activity: Edging towards cellular and synaptic mechanisms of working memory. *Neuroscience* **139**, 135–151 (2006).
17. Y. Burak, I. R. Fiete, Fundamental limits on persistent activity in networks of noisy neurons. *Proc. Natl. Acad. Sci. U.S.A.* **109**, 17645–17650 (2012).
18. M. E. Hasselmo, M. Sarter, Modes and models of forebrain cholinergic neuromodulation of cognition. *Neuropsychopharmacology* **36**, 52–73 (2011).
19. A. V. Egorov, B. N. Hamam, E. Fransén, M. E. Hasselmo, A. A. Alonso, Graded persistent activity in entorhinal cortex neurons. *Nature* **420**, 173–178 (2002).
20. B. Knauer, A. Jochems, M. J. Valero-Aracama, M. Yoshida, Long-lasting intrinsic persistent firing in rat CA1 pyramidal cells: A possible mechanism for active maintenance of memory. *Hippocampus* **23**, 820–831 (2013).
21. R. Andrade, Cell excitation enhances muscarinic cholinergic responses in rat association cortex. *Brain Res.* **548**, 81–93 (1991).
22. D. D. Fraser, B. A. MacVicar, Cholinergic-dependent plateau potential in hippocampal CA1 pyramidal neurons. *J. Neurosci.* **16**, 4113–4128 (1996).
23. R. Klink, A. Alonso, Muscarinic modulation of the oscillatory and repetitive firing properties of entorhinal cortex layer II neurons. *J. Neurophysiol.* **77**, 1813–1828 (1997).
24. K. Krnjević, R. Pumain, L. Renaud, The mechanism of excitation by acetylcholine in the cerebral cortex. *J. Physiol.* **215**, 247–268 (1971).
25. A. Arboit, A. Reboreda, M. Yoshida, Involvement of TRPC4 and 5 channels in persistent firing in hippocampal CA1 pyramidal cells. *Cells* **9**, 365 (2020).
26. E. Fransen, A. A. Alonso, M. E. Hasselmo, Simulations of the role of the muscarinic-activated calcium-sensitive nonspecific cation current INCM in entorhinal neuronal activity during delayed matching tasks. *J. Neurosci.* **22**, 1081–1097 (2002).
27. M. E. Hasselmo, Grid cell mechanisms and function: Contributions of entorhinal persistent spiking and phase resetting. *Hippocampus* **18**, 1213–1229 (2008).
28. M. Camperi, X. J. Wang, A model of visuospatial working memory in prefrontal cortex: Recurrent network and cellular bistability. *J. Comput. Neurosci.* **5**, 383–405 (1998).
29. C. P. Fall, J. Rinzel, An intracellular Ca2+ subsystem as a biologically plausible source of intrinsic conditional bistability in a network model of working memory. *J. Comput. Neurosci.* **20**, 97–107 (2006).
30. M. S. Goldman, J. H. Levine, G. Major, D. W. Tank, H. S. Seung, Robust persistent neural activity in a model integrator with multiple hysteretic dendrites per neuron. *Cereb. Cortex* **13**, 1185–1195 (2003).
31. C. Lin, V. N. Sherathiya, M. M. Oh, J. F. Disterhoft, Persistent firing in LEC III neurons is differentially modulated by learning and aging. *eLife* **9**, e56816 (2020).
32. S. D. Glasgow, T. A. J. Fisher, E. W. Wong, K. Lançon, K. M. Feighan, I. V. Beamish, J. Gibon, P. Séguéla, E. S. Ruthazer, T. E. Kennedy, Acetylcholine synergizes with netrin-1 to drive persistent firing in the entorhinal cortex. *Cell Rep.* **43**, 113812 (2024).
33. D. S. Olton, J. T. Becker, G. E. Handelmann, Hippocampus, space, and memory. *Behav. Brain Sci.* **2**, 313–322 (1979).
34. L. Nadel, L. MacDonald, Hippocampus: Cognitive map or working memory? *Behav. Neural Biol.* **29**, 405–409 (1980).
35. M. Sabariego, A. Schönwald, B. L. Boublil, D. T. Zimmerman, S. Ahmadi, N. Gonzalez, C. Leibold, R. E. Clark, J. K. Leutgeb, S. Leutgeb, Time cells in the hippocampus are neither dependent on medial entorhinal cortex inputs nor necessary for spatial working memory. *Neuron* **102**, 1235–1248.e5 (2019).
36. H. T. Ito, S.-J. Zhang, M. P. Witter, E. I. Moser, M.-B. Moser, A prefrontal–thalamo–hippocampal circuit for goal-directed spatial navigation. *Nature* **522**, 50–55 (2015).
37. D. Durstewitz, J. K. Seamans, T. J. Sejnowski, Neurocomputational models of working memory. *Nat. Neurosci.* **3**, 1184–1191 (2000).
38. M. Khona, I. R. Fiete, Attractor and integrator networks in the brain. *Nat. Rev. Neurosci.* **23**, 744–766 (2022).
39. J. S. Taube, J. P. Bassett, Persistent neural activity in head direction cells. *Cereb. Cortex* **13**, 1162–1172 (2003).
40. B. L. McNaughton, F. P. Battaglia, O. Jensen, E. I. Moser, M.-B. Moser, Path integration and the neural basis of the "cognitive map". *Nat. Rev. Neurosci.* **7**, 663–678 (2006).

41. B. Saber Marouf, A. Reboreda, F. Theissen, R. Kaushik, M. Sauvage, A. Dityatev, M. Yoshida, TRPC4 channel knockdown in the hippocampal CA1 region impairs modulation of beta oscillations in novel context. *Biology* **12**, 629 (2023).
42. P. S. Goldman-Rakic, Cellular basis of working memory. *Neuron* **14**, 477–485 (1995).
43. T. Spellman, M. Rigotti, S. E. Ahmari, S. Fusi, J. A. Gogos, J. A. Gordon, Hippocampal-prefrontal input supports spatial encoding in working memory. *Nature* **522**, 309–314 (2015).
44. M. Athanasiadis, S. Masserini, L. Yuan, D. Fetterhoff, J. K. Leutgeb, S. Leutgeb, C. Leibold, Low rate hippocampal delay period activity encodes behavioral experience. *Hippocampus* **34**, 422–437 (2024).
45. C. R. Quirk, I. Zutshi, S. Srikanth, M. L. Fu, N. Devico Marciano, M. K. Wright, D. F. Parsey, S. Liu, R. E. Siretskiy, T. L. Huynh, J. K. Leutgeb, S. Leutgeb, Precisely timed theta oscillations are selectively required during the encoding phase of memory. *Nat. Neurosci.* **24**, 1614–1627 (2021).
46. Y. Loewenstein, S. Mahon, P. Chadderton, K. Kitamura, H. Sompolinsky, Y. Yarom, M. Häusser, Bistability of cerebellar Purkinje cells modulated by sensory stimulation. *Nat. Neurosci.* **8**, 202–211 (2005).
47. J. Bröker-Lai, A. Kollewe, B. Schindeldecker, J. Pohle, V. Nguyen Chi, I. Mathar, R. Guzman, Y. Schwarz, A. Lai, P. Weißgerber, H. Schwegler, A. Dietrich, M. Both, R. Sprengel, A. Draguhn, G. Köhr, B. Fakler, V. Flockerzi, D. Bruns, M. Freichel, Heteromeric channels formed by TRPC1, TRPC4 and TRPC5 define hippocampal synaptic transmission and working memory. *EMBO J.* **36**, 2770–2789 (2017).
48. S. Lepannetier, R. Gualdani, S. Tempesta, O. Schakman, F. Seghers, A. Kreis, X. Yerna, A. Slimi, M. de Clippele, N. Tajeddine, T. Voets, R. S. Bon, D. J. Beech, F. Tissir, P. Gailly, Activation of TRPC1 channel by metabotropic glutamate receptor mGluR5 modulates synaptic plasticity and spatial working memory. *Front. Cell. Neurosci.* **12**, 318 (2018).
49. P. Vogel, J. Hahn, S. Duvarci, T. Sigurdsson, Prefrontal pyramidal neurons are critical for all phases of working memory. *Cell Rep.* **39**, 110659 (2022).
50. T. Leis, V. Pallage, G. Toniolo, B. Will, Working memory theory of hippocampal function needs qualification. *Behav. Neural Biol.* **42**, 140–157 (1984).
51. F. Cacucci, M. Yi, T. J. Wills, P. Chapman, J. O'Keefe, Place cell firing correlates with memory deficits and amyloid plaque burden in Tg2576 Alzheimer mouse model. *Proc. Natl. Acad. Sci. U.S.A.* **105**, 7863–7868 (2008).
52. D. G. Amaral, Emerging principles of intrinsic hippocampal organization. *Curr. Opin. Neurobiol.* **3**, 225–229 (1993).
53. J. J. Couey, A. Witoelar, S.-J. Zhang, K. Zheng, J. Ye, B. Dunn, R. Czajkowski, M.-B. Moser, E. I. Moser, Y. Roudi, M. P. Witter, Recurrent inhibitory circuitry as a mechanism for grid formation. *Nat. Neurosci.* **16**, 318–324 (2013).
54. E. K. Miller, C. A. Erickson, R. Desimone, Neural mechanisms of visual working memory in prefrontal cortex of the macaque. *J. Neurosci.* **16**, 5154–5167 (1996).
55. M. Noorman, B. K. Hulse, V. Jayaraman, S. Romani, A. M. Hermundstad, Maintaining and updating accurate internal representations of continuous variables with a handful of neurons. *Nat. Neurosci.* **27**, 2207–2217 (2024).
56. A. Jochems, M. Yoshida, A robust in vivo-like persistent firing supported by a hybrid of intracellular and synaptic mechanisms. *PLOS ONE* **10**, e0123799 (2015).
57. K. M. Gothard, W. E. Skaggs, K. M. Moore, B. L. McNaughton, Binding of hippocampal CA1 neural activity to multiple reference frames in a landmark-based navigation task. *J. Neurosci.* **16**, 823–835 (1996).
58. T. C. Foster, C. A. Castro, B. L. McNaughton, Spatial selectivity of rat hippocampal neurons: Dependence on preparedness for movement. *Science* **244**, 1580–1582 (1989).
59. K. Kay, M. Sosa, J. E. Chung, M. P. Karlsson, M. C. Larkin, L. M. Frank, A hippocampal network for spatial coding during immobility and sleep. *Nature* **531**, 185–190 (2016).
60. H. R. Joo, L. M. Frank, The hippocampal sharp wave-ripple in memory retrieval for immediate use and consolidation. *Nat. Rev. Neurosci.* **19**, 744–757 (2018).
61. J. O'Keefe, M. L. Recce, Phase relationship between hippocampal place units and the EEG theta rhythm. *Hippocampus* **3**, 317–330 (1993).
62. A. B. L. Tort, R. W. Komorowski, J. R. Manns, N. J. Kopell, H. Eichenbaum, Theta-gamma coupling increases during the learning of item-context associations. *Proc. Natl. Acad. Sci. U.S.A.* **106**, 20942–20947 (2009).
63. A. Reboreda, F. M. Theissen, M. J. Valero-Aracama, A. Arboit, M. A. Corbu, M. Yoshida, Do TRPC channels support working memory? Comparing modulations of TRPC channels and working memory through G-protein coupled receptors and neuromodulators. *Behav. Brain Res.* **354**, 64–83 (2018).
64. L. M. Teles-Grilo Ruivo, K. L. Baker, M. W. Conway, P. J. Kinsley, G. Gilmour, K. G. Phillips, J. T. R. Isaac, J. P. Lowry, J. R. Mellor, Coordinated acetylcholine release in prefrontal cortex and hippocampus is associated with arousal and reward on distinct timescales. *Cell Rep.* **18**, 905–917 (2017).
65. M. Sarter, V. Parikh, W. M. Howe, Phasic acetylcholine release and the volume transmission hypothesis: Time to move on. *Nat. Rev. Neurosci.* **10**, 383–390 (2009).
66. E. C. Ballinger, M. Ananth, D. A. Talmage, L. W. Role, Basal forebrain cholinergic circuits and signaling in cognition and cognitive decline. *Neuron* **91**, 1199–1218 (2016).
67. M. Wang, N. J. Gamo, Y. Yang, L. E. Jin, X.-J. Wang, M. Laubach, J. A. Mazer, D. Lee, A. F. T. Arnsten, Neuronal basis of age-related working memory decline. *Nature* **476**, 210–213 (2011).
68. M. M. Martin, D. G. Wallace, Selective hippocampal cholinergic deafferentation impairs self-movement cue use during a food hoarding task. *Behav. Brain Res.* **183**, 78–86 (2007).
69. P. L. Croxson, D. A. Kyriazis, M. G. Baxter, Cholinergic modulation of a specific memory function of prefrontal cortex. *Nat. Neurosci.* **14**, 1510–1512 (2011).
70. S. V. Puram, A. Riccio, S. Koirala, Y. Ikeuchi, A. H. Kim, G. Corfas, A. Bonni, A TRPC5-regulated calcium signaling pathway controls dendrite patterning in the mammalian brain. *Genes Dev.* **25**, 2659–2673 (2011).
71. S. N. Kadir, D. F. M. Goodman, K. D. Harris, High-dimensional cluster analysis with the masked EM algorithm. *Neural Comput.* **26**, 2379–2394 (2014).
72. S. Hattori, L. Chen, C. Weiss, J. F. Disterhoft, Robust hippocampal responsivity during retrieval of consolidated associative memory. *Hippocampus* **25**, 655–669 (2015).
73. W. Skaggs, B. McNaughton, K. Gothard, "An information-theoretic approach to deciphering the hippocampal code" in *Advances in Neural Information Processing Systems*, S. Hanson, J. Cowan, C. Giles, Eds. (Morgan-Kaufmann, 1992; https://proceedings.neurips.cc/paper_files/paper/1992/file/5dd9db5e033da9c6fb5ba83c7a7ebea9-Paper.pdf), vol. 5.
74. M. Guardamagna, F. Stella, F. P. Battaglia, Heterogeneity of network and coding states in mouse CA1 place cells. *Cell Rep.* **42**, 112022 (2023).
75. T. J. McHugh, K. I. Blum, J. Z. Tsien, S. Tonegawa, M. A. Wilson, Impaired hippocampal representation of space in CA1-Specific NMDAR1 knockout mice. *Cell* **87**, 1339–1349 (1996).
76. B. Phipson, G. K. Smyth, Permutation P-values should never be zero: Calculating exact P-values when permutations are randomly drawn. *Stat. Appl. Genet. Mol. Biol.* **9**, 39 (2010).
77. "Exploratory Data Analysis" in *The Concise Encyclopedia of Statistics* (Springer, New York, NY, 2008; https://link.springer.com/rwe/10.1007/978-0-387-32833-1_136), pp. 192–194.

Acknowledgments: We would like to thank K. Jeffery, S. Leutgeb, J. Leutgeb, M. Brandon, and K. Allen for their help in establishing the in vivo electrophysiological recordings. We thank L. Leichert and O. Stork for their assistance and technical support, and M. Freichel for sharing the TRPC KO mice with us. We thank M. Hasselmo, B. McNaughton, T. McHugh and S. Remy for their valuable comments on this manuscript. **Funding:** This work was supported by the Federal State of Saxony-Anhalt and the European Structural and Investment Funds (ESF, 2014–2020, project number ZS/2016/08/80645); the Deutsche Forschungsgemeinschaft projects YO177/4-1, YO177/4-3, and YO177/7-1 (to M.Y.); and the German Center for Neurodegenerative Diseases (to A.D.). **Author contributions:** Conceptualization: M.Y., M.S., and A.D. Analysis: A.R., M.Y., and B.S.M. Investigation: B.S.M., A.R., and F.T. Data curation: B.S.M. and A.R. Writing—original draft: M.Y. and A.R. Writing—review and editing: M.Y., A.R., and A.D. Methodology: A.D., R.K., M.Y., F.T., and M.S. Software: M.Y., B.S.M., and F.T. Visualization: A.R., M.Y., and B.S.M. Resources: A.D., M.S., R.K., and F.T. Validation: M.Y., A.R., M.S., and R.K. Funding acquisition: M.Y. and A.D. Supervision: M.Y., M.S., A.D., and R.K. Project administration: M.Y., M.S., and A.D. **Competing interests:** The authors declare that they have no competing interests. **Data, code, and materials availability:** All data needed to evaluate and reproduce the results in the paper are present in the paper and/or the Supplementary Materials. This study did not generate new materials. All code generated for the data analysis in this study is available at https://doi.org/10.5281/zenodo.21775727.

Submitted 12 February 2026
Accepted 24 September 2026
Published 30 October 2026
10.1126/sciadv.aef9907